Tracking dynamo mechanisms from local energy transfers: Application to the von Kármán sodium dynamo ⊘

M. Creff ✉ ⓘ ; H. Faller ⓘ ; B. Dubrulle ⓘ ; J.-L. Guermond ⓘ ; C. Nore ⓘ

Check for updates

CrossMark

View Online

Export Citation

Tracking dynamo mechanisms from local energy transfers: Application to the von Kármán sodium dynamo

View Online   Export Citation   CrossMark

M. Creff,[1,a]   H. Faller,[1,2]   B. Dubrulle,[2]   J.-L. Guermond,[3]   and C. Nore[1]

AFFILIATIONS

[1]Université Paris-Saclay, CNRS, LISN, 91400 Orsay, France
[2]Université Paris-Saclay, CEA, CNRS, 91191 Gif-sur-Yvette, France
[3]Department of Mathematics, Texas A&M University, 3368 TAMU, College Station, Texas 77843-3368, USA

[a]Author to whom correspondence should be addressed: melvin.creff@universite-paris-saclay.fr

ABSTRACT

Motivated by the observation that dynamo is a conversion mechanism between kinetic and magnetic energy, we develop a new approach to unravel dynamo mechanism based on local (in space, scale, and time) energy budget describing dissipation and scale-by-scale energy transfers. Our approach is based upon a new filtering approach that can be used effectively for any type of meshes, including unstructured ones. The corresponding formalism is very general and applies to any geometry or boundary conditions. We further discuss the interpretation of these energy transfers in the context of fast dynamo and anomalous dissipation. We apply it to the results from direct numerical simulations of the von Kármán Sodium setup (referred to as VKS) using a finite element code, showing dynamo action for two types of impellers (steel or soft iron) in the magnetic field growth and saturation phases. Although the two types of dynamo hardly differ from the mean-field theory point of view (the velocity fields are the same in both cases), the locality of our formalism allows us to trace the origin of the differences between these two types of dynamo: for steel impellers, the dynamo is due to the transfer of velocity energy both in the bulk and in the vicinity of the impellers, whereas for soft iron impellers, the dynamo effect mainly comes from the rotation of the blades. We finally discuss possible signatures of precursors to anomalous dissipation and fast dynamo, which could become relevant in the inviscid limit.

Published under an exclusive license by AIP Publishing. https://doi.org/10.1063/5.0174251

I. INTRODUCTION

In many natural systems, such as the Earth or the Sun, a large-scale magnetic field can be generated by the so-called dynamo process. Such a process is described via the magnetohydrodynamics (MHD) equations coupling the equations modeling incompressible viscous fluids (Navier–Stokes equations) with the equations modeling electromagnetism (Maxwell equations in the quasi-static approximation). Given the nonlinearities of the equations and the enormous range of scales involved in the process, it is very difficult to identify the main mechanisms allowing the generation of a magnetic field by the motion of an electrically conducting fluid. From a theoretical point of view, exact analytical results are generally only obtained in very simple geometries or by using symmetries to produce anti-dynamo conditions. Simplified models of dynamo generation can be built using mean field or stochastic approaches.[1,2] These approaches highlight the importance of helicity (via the so-called α-effect) and differential rotation (via the so-called Ω-effect) in the dynamo process. Such mean

field approach provided several possible dynamo scenarios, depending on which combination is chosen.[2] However, confronting such simple scenarios with numerical or experimental observation turns out to be very difficult. From a numerical point of view, simulations of MHD equations are only possible for a limited range of parameters, excluding the very turbulent situations observed in the liquid core of the Earth or in the plasma making up stars like the Sun. Moreover, the large amount of data and information makes it difficult to identify the relevant mechanisms at work in the dynamo action. From an experimental point of view, the situation is the opposite: using liquid metal experiments, it is possible to reach very turbulent regimes. However, owing to the difficulty of measurements, it is only possible to produce sparse data that are not detailed enough to enable the identification of dynamo mechanisms, except in some special situations where the geometry is very constrained and the mean flow of liquid sodium reproduces analytical examples[3,4] in the linear phase of the (kinematic) dynamo.

The von Kármán flow experiment using liquid sodium (hereafter referred to as VKS for von Kármán Sodium) is a good example of such difficulties. The facility uses 150 liters of liquid sodium that are set in turbulent motion by two counter-rotating impellers in a cylindrical container.[5] During its 16 years of operations, the VKS facility produced dynamo onset only with (i) impellers made of soft iron,[5] and not with cooper or steel, (ii) for fluid motions with limited fluctuations.[6] This last observation rules out the possibility that the VKS dynamo is a mere rotating magnet. It also suggests that velocity fluctuations may impede the dynamo process, as already proved by dedicated numerical simulations in a simple geometry[7] or asymptotics.[6,8] Various attempts have been made to explain such results within the mean-field framework. For example, Petrelis, Mordant, and Fauve suggested a possible $\alpha - \Omega$ mechanism for the dynamo, based on the combination of eddies generated near the impellers, and differential rotation,[9] a scenario confirmed by numerical simulations of a simplified model of the velocity field[10] or RANS simulations of the von Kármán flow.[11] This model however does not explain the important influence of the iron impellers on the dynamo onset. Additional physical processes were then invoked such as the interplay between the Ω effect and a new conversion effect linked with spatially varying electrical conductivity[12–14] or magnetic permeability.[15–18] Finally, enhancement of the α effect via eddy collimation by the impeller magnetic field was discussed in Refs. 19 and 20.

Detailed verification of these hypotheses is difficult in the context of the mean-field model since it is a large-scale model where all the small-scale action is parameterized in the coefficients α and Ω. Here, we propose a new approach to unravel these mechanisms, motivated by the observation that dynamo is a conversion mechanism between kinetic and magnetic energy. The core of our approach is based on local (in space, scale and time) energy budget describing dissipation and scale-by-scale energy transfers. Identifying the locations (in scale, space, and time) where kinetic and magnetic energies are exchanged supplies information about the location of the dynamo effect. Comparison with local magnetic or energy dissipation then tells us whether the conversion is sufficient to overcome damping, and thus, sustain dynamo action. The formalism is very general and applies to any geometry or boundary conditions. Then, by applying it to the case of the VKS dynamo, we show how it can be used to detect where and when the energy conversion between kinetic and magnetic energy takes place, thereby tracing the processes at work in the dynamo. Specifically, we use the massively parallel multiphysics code called SFEMaNS (for Spectral/Finite Element code for Maxwell and Navier–Stokes equations). This code solves the magnetohydrodynamics equations (MHD) describing the time evolution of the velocity and magnetic fields in the von Kármán sodium experiment. With this code two types of dynamo action have been explored: one using soft iron impellers and the other using steel impellers.[21] Although the two types of dynamo hardly differ from the mean-field theory point of view (the velocity fields are the same in both cases), the locality of our formalism allows us to trace the origin of the differences between these two types of dynamo.

The paper is organized as follows. The coupled equations describing the motion of a conducting fluid are presented in Sec. II. We first recall elements of basic mean-field theory, focusing on typical α and Ω dynamo mechanisms. In Sec. III, we present our new formalism, based on the derivation of local energy budgets from the MHD equations.

We first build coarse-grained energy budgets including inertial dissipation, anomalous dissipation, and transfer terms between velocity and magnetic fields. Taking the limit of infinite resolution, we discuss the exact energy budgets with no filter. The generalization of the famous Kolmogorov 4/3rd law is presented in this context. A crucial ingredient for application of the formalism is the notion of scale filtering. Traditional definitions of scale filtering, through convolution with a filter, are not suitable for unstructured grids. We, therefore, define a suitable filtering process that applies to any type of grid and boundary conditions, including the unstructured grid used in our numerical simulations in Sec. III E. This formalism is applied to the numerical simulations of the dynamo in the von Kármán geometry that are presented in Sec. IV B (and detailed in Subsections 1–3 of Appendix E). We discuss the standard dynamo mechanisms based on the mean-field theory in Sec. IV C. In Sec. V, we use the energy budgets to unravel the dynamo mechanisms at work in the VKS experiment for impellers with different magnetic permeabilities. The same tools are used to study the saturation of the dynamo in Sec. VI. Using these results, we discuss in Sec. VII the mechanisms for dynamo action in the VKS experiment and compare them with the literature. Our conclusion follows in Sec. VIII.

II. BACKGROUND MATERIAL AND GENERAL FORMALISM

A. Magnetohydrodynamics equations

The magnetohydrodynamics equations (MHD) for a neutral conductive incompressible Newtonian fluid in the quasi-static approximation are

$$\partial_t u + \partial_i(u_i u) - \nu \Delta u + \frac{\nabla p}{\rho} = -\frac{b \times j}{\rho} + f, \tag{1}$$

$$\partial_t b = \nabla \times (u \times b) - \nabla \times \frac{j}{\sigma}, \tag{2}$$

$$\nabla \cdot u = 0, \tag{3}$$

$$\nabla \cdot b = 0, \tag{4}$$

$$j = \nabla \times H, \tag{5}$$

$$b = \mu H, \tag{6}$$

where H is the magnetic field, b the magnetic flux density (i.e., magnetic induction that we will abusively call magnetic field in the following), j the electric current density, u the fluid velocity (with u_i one of its components with $i \in \{1, 2, 3\}$), p the fluid pressure, f the force per unit mass, μ the magnetic permeability, σ the electric conductivity, ν the kinematic viscosity, and ρ the fluid density. The space and time dependence of all fields has been removed in the notations for convenience except when necessary.

B. Mean field theory: α and Ω effects

We briefly summarize classical mean-field concepts that are traditionally used to interpret numerical results and to understand the basic dynamo mechanisms. For the sake of simplicity, it is assumed here that σ and μ do not vary in space nor in time. Therefore, Eq. (2) reads

$$\partial_t b = \nabla \times (u \times b) + \frac{1}{\mu \sigma} \nabla^2 b. \tag{7}$$

We consider b and u as superimpositions of mean and fluctuating parts such that $b = \overline{b} + b'$ and $u = \overline{u} + u'$ where $\overline{b}, \overline{u}$ can have

smooth variations in space and time. Injecting these decompositions into Eq. (7) and taking its average, we get

$$\partial_t \overline{b} = \nabla \times (\overline{u} \times \overline{b} + \text{emf}) + \frac{1}{\mu\sigma} \nabla^2 \overline{b} \quad \text{with } \nabla \cdot \overline{b} = 0, \quad (8)$$

where emf $= \langle u' \times b' \rangle$ is the mean electromotive force due to the fluctuations of motion and magnetic field. These equations together with proper initial and boundary conditions determine $\overline{b}$ if $\overline{u}$ and emf are given. The determination of the mean electromotive force as a function of $u', \overline{b}, \overline{u}$ is the crucial step in the development of mean-field theory. For the sake of simplicity, we focus only on a low magnetic Prandtl situation $\nu\mu\sigma \ll 1$, relevant to a fluid such as liquid metal. In such a case, we can consider that the dynamics of the magnetic fluctuations b' is dominated by the interaction of the velocity fluctuations u' with the mean magnetic field $\overline{b}$ only. This means that

$$\partial_t b' \simeq \nabla \times (u' \times \overline{b}) = (\overline{b} \cdot \nabla)u' - (u' \cdot \nabla)\overline{b}. \quad (9)$$

This fluctuating magnetic field is used to compute the electromotive force as detailed in Ref. 2

$$\text{emf}_i = \alpha_{ij}\overline{b}_j + \beta_{ijk}\partial\overline{b}_j/\partial x_k, \quad (10)$$

where the tensors α_{ij} and β_{ijk} are mean quantities determined by u'. The α-effect is the occurrence of a mean electromotive force with a component pointing in the direction of the mean magnetic field $\overline{b}$. Based on results from Ref. 11, we will focus on this effect and discard the β tensor. Approximating the fluctuations by a short in-time field (supposing a short turbulence correlation time), one can link the α tensor to the helicity tensor as

$$\alpha_{ij} = \tau h_{ij} = \tau \varepsilon_{ikn} u_k (\nabla u)_{nj}, \quad (11)$$

where τ is the correlation time of the velocity perturbations, ε_{ikn} is the Levi-Civita tensor, and ∇u is the velocity gradient expressed in cylindrical coordinates (see Subsection 4 of Appendix E).

Another conversion mechanism is due to differential rotation. Indeed, using the cylindrical coordinate system, the induction Eq. (7) can be written as

$$\left[\frac{\partial}{\partial t} + u_r \frac{\partial}{\partial r} + \frac{u_\theta}{r}\frac{\partial}{\partial \theta} + u_z \frac{\partial}{\partial z}\right] b_r$$
$$= \left[b_r \frac{\partial}{\partial r} + \frac{b_\theta}{r}\frac{\partial}{\partial \theta} + b_z \frac{\partial}{\partial z}\right] u_r + \frac{1}{\mu\sigma}\left[\Delta_* b_r - \frac{2}{r^2}\frac{\partial b_\theta}{\partial \theta}\right], \quad (12)$$

$$\left[\frac{\partial}{\partial t} + u_r \left(\frac{\partial}{\partial r} - \frac{1}{r}\right) + \frac{u_\theta}{r}\frac{\partial}{\partial \theta} + u_z \frac{\partial}{\partial z}\right] b_\theta$$
$$= \left[b_r r\frac{\partial}{\partial r} + b_\theta \frac{\partial}{\partial \theta} + b_z r\frac{\partial}{\partial z}\right]\left(\frac{u_\theta}{r}\right) + \frac{1}{\mu\sigma}\left[\Delta_* b_\theta + \frac{2}{r^2}\frac{\partial b_r}{\partial \theta}\right], \quad (13)$$

$$\left[\frac{\partial}{\partial t} + u_r \frac{\partial}{\partial r} + \frac{u_\theta}{r}\frac{\partial}{\partial \theta} + u_z \frac{\partial}{\partial z}\right] b_z$$
$$= \left[b_r \frac{\partial}{\partial r} + \frac{b_\theta}{r}\frac{\partial}{\partial \theta} + b_z \frac{\partial}{\partial z}\right] u_z + \frac{1}{\mu\sigma}\nabla^2 b_z, \quad (14)$$

with $\Delta_* = \nabla^2 - \frac{1}{r^2} = \frac{\partial^2}{\partial r^2} + \frac{1}{r}\frac{\partial}{\partial r} + \frac{1}{r^2}\frac{\partial^2}{\partial\theta^2} + \frac{\partial^2}{\partial z^2} - \frac{1}{r^2}$. This form of the induction equation clearly shows that, if the poloidal magnetic field, i.e., $\{b_r, b_z\}$, is non-zero, its shearing by the differential rotation

(u_θ/r) will always generate a toroidal magnetic field, i.e., b_θ. This mechanism is called the Ω-effect. Denoting the two main terms in the rhs of (13)

$$\Omega'_r = \frac{\partial}{\partial r}\left(\frac{u_\theta}{r}\right), \quad \Omega'_z = \frac{\partial}{\partial z}\left(\frac{u_\theta}{r}\right),$$

one can see that the source terms for the toroidal field are $b_r r \Omega'_r$ and $b_z r \Omega'_z$.

The dynamo effect is due to a combination of poloidal and toroidal magnetic field generation mechanisms, in the form of closing loops. Therefore, different dynamo mechanisms can be conceived: there is a possibility for the poloidal magnetic field $\{b_r, b_z\}$ to be generated from the toroidal field b_θ through the α-effect. To close the loop and generate further toroidal field from such poloidal field, there are two possibilities (possibly concomitant): either through the α-effect or (and) the mean differential rotation $r\Omega'_z$ and $r\Omega'_r$. The corresponding dynamo loops are then, respectively, called α^2 dynamo or $\alpha - \Omega$ dynamo.

III. LOCAL ENERGY BUDGET

In order to evaluate the energy budgets describing relevant transfers of energy between the magnetic and velocity fields, we use a filtering approach and consider products of resolved and non-resolved quantities. This strategy is inspired by the mathematical derivation of anomalous dissipation due to the irregularities of (i) velocity field in the context of the Navier–Stokes equations[22] and (ii) velocity and magnetic fields in the context of the magnetohydrodynamics equations.[23,24] Our work extends these studies by introducing possible variations of the material properties (μ, σ). This is important in order to deal with the physical quantities resulting from the simulations presented in Subsections 1–3 of Appendix E and to evaluate the impact of jumps in electrical conductivity σ and magnetic permeability μ.

A. Filtered equations

To characterize the energy transfers between scales of the same vector field, we use a filtering process in order to distinguish between the energy held by the different scales of the field. Given a vector field u and $\ell \in \mathbb{R}^+$, we denote its filtered field $\overline{u}^\ell$. At the present time, we do not specify the shape of the filter that is just assumed to obey the following properties: linearity, and such that $\overline{u}^\ell \xrightarrow{\ell \to 0} u$ for a smooth field u.

Applying the filter to the MHD Eqs. (1) and (2), we get

$$\partial_t \overline{u}^\ell + \partial_i \overline{u_i u}^\ell - \nu\Delta\overline{u}^\ell + \frac{\nabla\overline{p}^\ell}{\rho} = -\frac{\overline{b \times j}^\ell}{\rho} + \overline{f}^\ell, \quad (15)$$

$$\partial_t \overline{b}^\ell = \nabla \times (\overline{u \times b}^\ell) - \nabla \times \overline{\left(\frac{j}{\sigma}\right)}^\ell, \quad (16)$$

$$\nabla \cdot \overline{u}^\ell = 0, \quad (17)$$

$$\nabla \cdot \overline{b}^\ell = 0. \quad (18)$$

Because the density and the viscosity of the fluid are constant in our simulations, they do not impact the filtering and can be taken out of the convolution.

B. Local MHD coarse-grained energy budget at finite scale ℓ

Summing the scalar product of $\rho u/2$ with Eq. (15) and the scalar product of $\rho \overline{u}^\ell/2$ with Eq. (1) and using analogous products for b, the equations for the filtered kinetic energy $E^c = \frac{\rho u \overline{u}^\ell}{2}$ and filtered magnetic energy $E^m = \frac{b \overline{b}^\ell}{2\mu}$ can be respectively written as

$$\partial_t E^c + \nabla \cdot J^{NS} + \mathcal{D}^\nu + \mathcal{D}^u + \mathcal{D}^b = -\mathcal{T}^{u \to b} + \mathcal{P}, \quad (19)$$

$$\partial_t E^m + \nabla \cdot J^M + \mathcal{D}^\sigma + \mathcal{D}^{\overline{\sigma}} + \mathcal{D}^b + \mathcal{D}^{\mu\sigma} + \mathcal{D}^{\mu\mathcal{T}} = \mathcal{T}^{u \to b} + \mathcal{M}^\mu, \quad (20)$$

with

$$J^{NS} = \frac{\rho}{2}\left((u\overline{u}^\ell)u - \nu\nabla(u\overline{u}^\ell)\right) + \frac{1}{2}\left(\overline{u}^\ell p + u\overline{p}^\ell\right), \quad (21)$$

$$J^M = \frac{1}{2\mu}\left\{ \frac{j}{\sigma} \times \overline{b}^\ell + \overline{\left(\frac{j}{\sigma}\right)}^\ell \times b + b \times \overline{(u \times b}^\ell) + \overline{b}^\ell \times (u \times b) \right\}, \quad (22)$$

$$\mathcal{P} = \frac{\rho}{2}\left(u \cdot \overline{f}^\ell + \overline{u}^\ell \cdot f\right), \quad (23)$$

$$\mathcal{D}^\nu = \rho\nu\partial_i\overline{u_j}^\ell\partial_i u_j, \quad (24)$$

$$\mathcal{D}^\sigma = \frac{j \cdot \overline{j}^\ell}{\sigma}, \quad \mathcal{D}^{\overline{\sigma}} = \left(\overline{\left(\frac{j}{\sigma}\right)}^\ell - \frac{(\overline{j}^\ell)}{\sigma}\right) \cdot \frac{j}{2}, \quad (25)$$

$$\mathcal{D}^u = \frac{\rho}{2}\left(u\overline{u_i\partial_i u}^\ell - u u_i\partial_i\overline{u}^\ell\right), \quad (26)$$

$$\mathcal{D}^b = \frac{1}{4}\left(\overline{u}^\ell \cdot (b \times j) + u \cdot \overline{(b \times j}^\ell) - \overline{(u \times b}^\ell) \cdot j - (u \times b) \cdot \overline{j}^\ell\right), \quad (27)$$

$$\mathcal{T}^{u \to b} = \frac{1}{4}\left(\overline{u}^\ell \cdot (b \times j) + u \cdot \overline{(b \times j}^\ell) + \overline{(u \times b}^\ell) \cdot j + (u \times b) \cdot \overline{j}^\ell\right), \quad (28)$$

$$\mathcal{M}^\mu = -\frac{b \cdot \overline{b}^\ell}{2\mu^2}\partial_t\mu, \quad (29)$$

$$\mathcal{D}^{\mu\sigma} = \frac{j}{2\sigma} \cdot \nabla \times \left(\frac{(\overline{b}^\ell)}{\mu} - \overline{H}^\ell\right), \quad (30)$$

$$\mathcal{D}^{\mu\mathcal{T}} = -\frac{(u \times b)}{2} \cdot \nabla \times \left(\frac{(\overline{b}^\ell)}{\mu} - \overline{H}^\ell\right).$$

All terms involved in Eqs. (19) and (20) measure the transferred energy from all scales larger than ℓ to the scale ℓ. By convention, we do not use a subscript ℓ for all terms in contrast with Refs. 23, 25, and 26. The demonstration for (19) [respectively (20)] is in Appendix A (respectively in Appendix B).

We first discuss the different terms appearing in Eq. (19). On the left-hand side (lhs), J_{NS} represents an energy current responsible for the spatial movement of energy and thus does not participate in any kind of dissipation or transfer of energy between the different scales. Integrated throughout space with the proper boundary conditions, it should disappear. $\mathcal{D}^\nu$ is the dissipation due to the kinematic viscosity: it corresponds to a loss of energy of the velocity field. $\mathcal{D}^u$ is the anomalous/Duchon–Robert dissipation. This term is the local energy transfer

at scale ℓ and thus characterizes where the irregularities, and possible singularities, appear in the fields. It is called anomalous dissipation because, in the limit $\ell \to 0$, $\mathcal{D}^u$ might not vanish.[22] These two different energy transfers ($\mathcal{D}^\nu$ and $\mathcal{D}^u$) have already been derived and implemented in the SFEMaNS code (see Subsection 2 of Appendix E) in order to study their effects in a pure hydrodynamic problem modeled by the Navier–Stokes equations.[27] $\mathcal{D}^b$ is a transfer term between different scales due to the interplay between velocity u and magnetic induction b fields. Like in the kinetic case, such a term could also produce an anomalous contribution to the magnetic energy budget in case the velocity field or the magnetic induction field is sufficiently irregular. If the contribution is positive, the net effect would then be an anomalous dissipation, like in the kinetic case. However, there is also the possibility that the contribution is negative, resulting in an increase in the magnetic energy due to irregularity. This would correspond to a scenario by which a dynamo is produced via a sufficiently rough velocity field,[28] a mechanism known as fast dynamo mechanism.[29]

The first right-hand side (rhs) term ($-\mathcal{T}^{u \to b}$) corresponds to the power of the Lorentz force and reflects an energy transformation between the fields u and b. It naturally appears with the opposite sign in the rhs of the magnetic energy budget (20) and is, therefore, responsible for the emergence and maintenance of the magnetic field. In other words, $\mathcal{T}^{u \to b}$ is a source term for the dynamo effect. The second term, $\mathcal{P}$, displays the mechanical power injected by the forcing.

Aside the $\mathcal{T}^{u \to b}$ term, new interesting energy transfer terms appear in (20). In the lhs part, as before, J_M is a purely local term that describes how magnetic energy is transported across the flow, and it should vanish after integration over space with the appropriate boundary conditions. $\mathcal{D}^\sigma$ is the Joule dissipation; hence, a loss of energy of the magnetic field, and can be used to trace, locally and across scales, the rate of resistive energy dissipation. $\mathcal{D}^{\overline{\sigma}}$ has contributions only where the electrical conductivity undergoes jumps, i.e., at $\{r = 1.4, \, 0 \le \theta < 2\pi, \, -1 \le z \le 1\}$ between the liquid sodium steady layer and the copper wall of the container [see Fig. 1(a)]. $\mathcal{D}^{\mu\sigma}$ and $\mathcal{D}^{\mu\mathcal{T}}$ are two terms associated with the irregularity of the magnetic permeability μ which occurs only at the surface of the impellers. They are respectively denoted Joule induced in-between scales magnetic transfer and Lorentz induced in-between scales magnetic transfer. Finally, in the rhs part, another source term for the dynamo effect appears, namely, $\mathcal{M}^\mu$, which we will call the magnet effect. It originates from the variation in time of the magnetic permeability and is a direct energy transfer from the impellers to the magnetic field.

C. Exact local MHD energy budget

The exact local energy budget can be obtained by taking the limit $\ell \to 0$. A technical difficulty may arise if the field is sufficiently irregular. In that case, terms corresponding to energy transfer may not need to vanish, producing anomalous dissipation of kinetic energy[22] or magnetic energy,[30,31] or even dynamo action.[28]

In the case where the field is sufficiently regular, so that these terms vanish, the time evolution for the kinetic and magnetic energies (per unit volume) simplifies to

$$\partial_t \frac{\rho u^2}{2} + \nabla \cdot J_0^{NS} + \mathcal{D}_0^\nu = -\mathcal{T}_0^{u \to b} + \mathcal{P}_0, \quad (31)$$

$$\partial_t \frac{b^2}{2\mu} + \nabla \cdot J_0^M + \mathcal{D}_0^\sigma = \mathcal{T}_0^{u \to b} + \mathcal{M}_0^\mu, \quad (32)$$
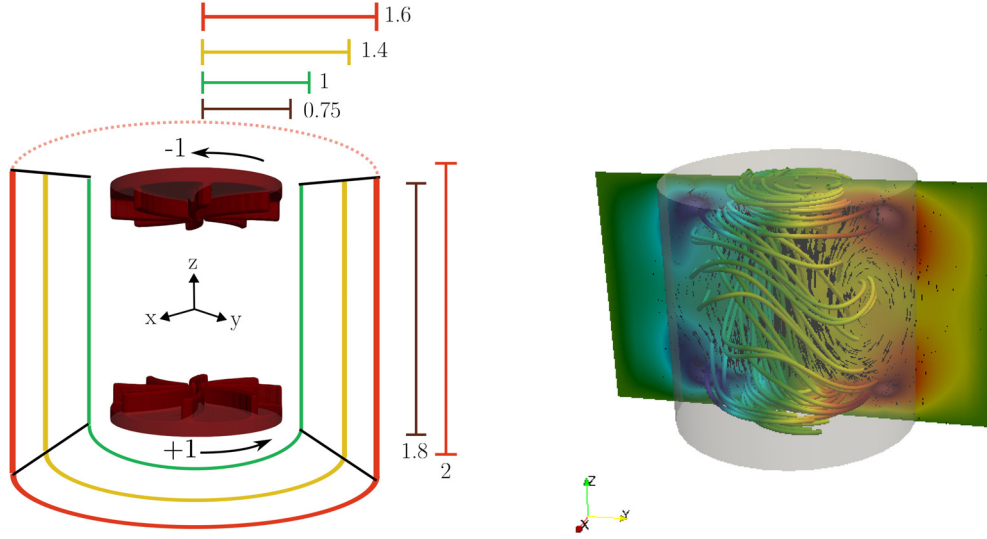
with

FIG. 1. (a) Schematic of the VKS experimental device of Ref. 5 in non-dimensional units. The impellers counter-rotate as indicated. (b) Magnetohydrodynamics simulation of the von Kármán Sodium dynamo at kinetic Reynolds number $R_e = 1500$, magnetic Reynolds number $R_m = 150$ and relative magnetic permeability of the impellers $\mu_r = 50$: visualization of the time-averaged magnetic field lines and section of the azimuthal magnetic field component. Adapted from Ref. 21.

$$J_0^{NS} = \frac{\rho}{2}\left(u^2 u - \nu \nabla u^2\right) + up, \tag{33}$$

$$J_0^M = \frac{1}{\mu}\left\{ \frac{j}{\sigma} \times b + b \times (u \times b) \right\}, \tag{34}$$

$$\mathcal{D}_0^\nu = \rho\nu\partial_i u_j \partial_i u_j, \quad \mathcal{D}_0^\sigma = \frac{j^2}{\sigma}, \tag{35}$$

$$\mathcal{T}_0^{u\to b} = u \cdot (b \times j), \quad \mathcal{M}_0^\mu = -\frac{b^2}{2\mu^2}\partial_t\mu, \quad \mathcal{P}_0 = \rho u \cdot f. \tag{36}$$

As before, the J terms represent energy current responsible for the spatial displacement of energy and do not participate in transfers. The terms $\mathcal{D}_0^\nu$ and $\mathcal{D}_0^\sigma$ are the standard viscous and resistive dissipation terms respectively. The right-hand side of (32) shows the two dynamo source terms, namely, (minus) the Lorentz force power and the magnet effect and the rhs of (31) shows the Lorentz force power and the mechanical power due to the forcing.

Note that in the case where the velocity and/or magnetic induction fields are irregular, other terms should be considered in the energy budget, due to the non-vanishing of terms like $\mathcal{D}^u$, $\mathcal{D}^b$, $\mathcal{D}^{\mu\sigma}$, and $\mathcal{D}^{\mu\mathcal{T}}$ in the limit $\ell \to 0$ in Eqs. (19) and (20).

D. Definition of a local dynamo growth rate

We can use the energy budgets to define a global dynamo growth rate at several scales. Indeed the rhs of Eq. (20) evidence two possible source terms for the increase in the magnetic energy: the source term already discussed $\mathcal{T}^{u\to b}$ and the $\mathcal{M}^\mu$ term that exists only in case where permeability varies in time (This will be the case for example in the von Kármán setup if the impellers are made of permeable material such as for example, soft iron[5]) This last term is called in the sequel the "rotating magnet effect." Physically, the sum of these two terms must exceed the sum of all dissipative terms in the lhs of Eq. (20) for the dynamo to operate.

This can be formalized with the local growth rate $\lambda^m(\vec{x}, t)$ of the magnetic field at scale ℓ given by

$$\lambda^m = \frac{\mathcal{T}^{u\to b} + \mathcal{M}^\mu - \mathcal{D}^\sigma - \mathcal{D}^{\bar\sigma} - \mathcal{D}^b - \mathcal{D}^{\mu\sigma} - \mathcal{D}^{\mu\mathcal{T}}}{\langle E^m\rangle}, \tag{37}$$

where $\langle.\rangle$ denotes the spatial average. Therefore, the evolution of the filtered magnetic energy (20) can be recast into

$$\partial_t E^m + \nabla \cdot J^M = \lambda^m \langle E^m\rangle. \tag{38}$$

For $\ell \to 0$, the growth rate can have two types of behavior. For the first one, the field is sufficiently regular, in which case all transfer terms between scales vanish, and the local growth rate is simply

$$\lambda_0^m = \frac{\mathcal{T}_0^{u\to b} + \mathcal{M}_0^\mu - \mathcal{D}_0^\sigma}{\langle E^m\rangle}. \tag{39}$$

This case will correspond to numerical simulations as no singularity can develop there because of the finite resolution. For the second type of behavior, in natural or experimental cases, there may be a contribution from the terms like $\mathcal{D}^{\bar\sigma}$, $\mathcal{D}^b$, etc., resulting in a possibility of dynamo generation by singularity if these terms are negative. This is the case discussed in Ref. 28.

E. Implementation of the scale filtering

As the construction of local energy budgets relies heavily on the notion of filtering, we present a general definition that is appropriate for any type of grid or boundary conditions. Classical definitions of scale filtering involve the convolution of a quantity with a filter of appropriate width (generally a Gaussian field). For data defined on homogeneous grid, like experimental data considered in Refs. 25 and 32, this definition is easily implemented via wavelet transforms. For data defined on unstructured grids, the wavelet construction is not

appropriate. We, therefore, consider here another construction, which can be adapted to any type of grid or boundary conditions. Given a vector field u and $\ell \in \mathbb{R}^+$, we define the filtered field $g = \overline{u}^\ell$ as the solution of

$$g - \ell^2 \Delta g = u. \tag{40}$$

This definition ensures that it can be constructed for any type of grid and is easy to implement inside a numerical program. Moreover, it is endowed with all properties of a classical filter: it is linear and, for a continuous field u, we have the limit $\overline{u}^\ell \xrightarrow{\ell \to 0} u$. In fact, this filter corresponds to a convolution filter. Indeed, in Fourier space, Eq. (40) reads

$$\tilde{g} = \frac{\tilde{u}}{1 + \ell^2 k^2}, \tag{41}$$

where $\tilde{g}$ is the Fourier transform of g. Thus, $\overline{u}^\ell$ is the convolution of u with the inverse Fourier transform of the Lorentzian function $\frac{1}{1 + \ell^2 k^2}$.

F. Connection with previous works

Our formalism can be connected to previous works by introducing $\delta_\ell u$, the longitudinal velocity increment at scale ℓ, defined as

$$\delta_\ell u = \hat{\ell} \cdot (\mathbf{u}(\mathbf{x} + \ell, t) - \mathbf{u}(\mathbf{x}, t)), \tag{42}$$

where $\hat{\ell}$ is the increment unit vector.

In Ref. 23, Galtier derives the local energy conservation in incompressible Hall MHD equations when the velocity and magnetic fields are possibly non-regular. He focuses on the time evolution of the total energy $E^c + E^m$ for a plasma with constant electrical conductivity and magnetic permeability, corresponding to the sum of Eqs. (19) and (20). As a result, the source term $\mathcal{T}^{u \to b}$ disappears together with all terms depending on the variation of σ and μ (namely, $\mathcal{M}^\mu$, $\mathcal{D}^{\overline{\sigma}}$, $\mathcal{D}^{\mu\sigma}$, $\mathcal{D}^{\mu T}$). The energy dissipation by viscous and resistive effects is then reduced to one term $\mathcal{D}^\nu + \mathcal{D}^\sigma$. In the same way, the energy transfer term becomes lumped into mixed terms, involving both u and b, which does not allow separating the various source terms. The final energy budget can then be written using the notations of Ref. 23 [see Eq. (22) therein with the ion skin depth $d_I = 0$] as

$$
\begin{aligned}
\mathcal{D}_\varepsilon &= \frac{1}{4} \int (\nabla \varphi_\ell) \cdot (\delta u \delta u^2 + \delta u \delta b^2 - 2(\delta u \cdot \delta b)\delta b) d\vec{r} \\
&= S^{NS} + \tilde{S}^{Mag} \\
&= \frac{1}{\rho} \mathcal{D}^u + 2\mu \mathcal{D}^b + \frac{1}{2} \nabla \cdot (J_{S^{Mag}} + J_{S^{NS}}),
\end{aligned} \tag{43}
$$

where S^{NS} (respectively $\tilde{S}^{Mag}$) and $J_{S^{NS}}$ (respectively $J_{S^{Mag}}$) are defined in Appendix C (respectively Appendix D). Therefore, our analysis has a direct link with previous works,[23,31] with the advantage that tracking E^c and E^m separately allows to get insights into the dynamo effect, as we now show.

IV. THE VON KÁRMÁN DYNAMO
A. Generality

We now apply these results to the analysis of the von Kármán dynamo. This dynamo is an example of a turbulent dynamo. It was first observed experimentally in 2006 in a von Kármán swirling flow of liquid sodium (called VKS[5]) for a magnetic Reynolds number larger

than $R_m^c = 34$. The dynamo at saturation takes the shape of a dominantly dipolar axisymmetric magnetic field with a toroidal magnetic field concentrated in the impellers.[5] MHD simulations of the von Kármán setup have been performed on various supercomputers[21] (up to about 2000 cores on the IDRIS supercomputer), allowing us to reach kinetic Reynolds number up to 10^5 and magnetic Reynolds number of the order of a few hundred, resulting in a magnetic Prandtl number around 10^{-3}. This is larger than the experimental value, which is of the order $5\,10^{-6}$. Despite this, several key features of the magnetic field dynamo observed in the VKS experiment were recovered. The MHD simulations showed the key role played by the ferromagnetic material (with high magnetic permeability) constituting the impellers. When soft iron impellers are modeled using a relative magnetic permeability $\mu_r = 50$, the magnetic field is dominated by an axisymmetric axial dipole and azimuthal components located near the impellers in agreement with the experimental data [see Fig. 1(b) adapted from Ref. 21] A similar dominant axisymmetric magnetic field was also observed at $R_e = 2025$ and a magnetic Prandtl number of 1/3 for $\mu_r \simeq 12$ in Ref. 33.

B. Description of the numerical data

Details of numerical runs are reported in Subsections 1–3 of Appendix E. The non-dimensionalized computational domain for the hydrodynamic study is $\Omega = \{(r, \theta, z) \in [0, 1] \times [0, 2\pi] \times [-1, 1]\}$. The computational domain for the MHD study is the larger cylinder $\Omega \cup \Omega_{out}$ with $\Omega_{out} = \{(r, \theta, z) \in [1, 1.6] \times [0, 2\pi] \times [-1, 1]\}$ [see schematic on Fig. 1(a)]. The electrical conductivity is that of the liquid sodium for $0 \leq r \leq 1.4$ and that of copper for $1.4 \leq r \leq 1.6$. The characteristics of the runs used in this paper are summarized in Table I. We use R_m values above the respective threshold. Each regime is sampled with 128 snapshots (every one-eighth of a turn to stroboscope the impellers' motion). We denote the average on all the snapshots as $\{.\}$.

C. Analysis using the mean-field framework

The von Kármán dynamo has been extensively discussed using the classical mean-field framework.[9–11,19,20] For later reference, we apply this framework to the two different dynamos considered here by computing in each case the local helicity tensor using the velocity field averaged on the 128 snapshots. They are shown on Figs. 2 and 3. Their spatial distribution is complex and exhibits fine scales. Note that the dominant patterns of each local helicity component follow the symmetry rules detailed in Subsection 4 of Appendix E [see Eq. (E6)]. This means that the large structures of the velocity field are mainly R_π symmetric at $R_e = 1500$ for both μ_r values.

We can see that the maxima in absolute value are always localized near the impellers like in the RANS simulation of Ref. 11 whereas the

TABLE I. Characteristics of two dynamo runs (DNS): kinetic Reynolds number $R_e = R_{cyl}^2 \omega / \nu$, magnetic Reynolds number $R_m = \mu_0 \sigma_0 R_{cyl}^2 \omega$, relative magnetic permeability of impellers μ_r (1 for stainless steel and 50 for soft-iron), critical magnetic Reynolds number for pseudo-vacuum boundary conditions (i.e., the tangential components of H are zero on the outer cylinder).

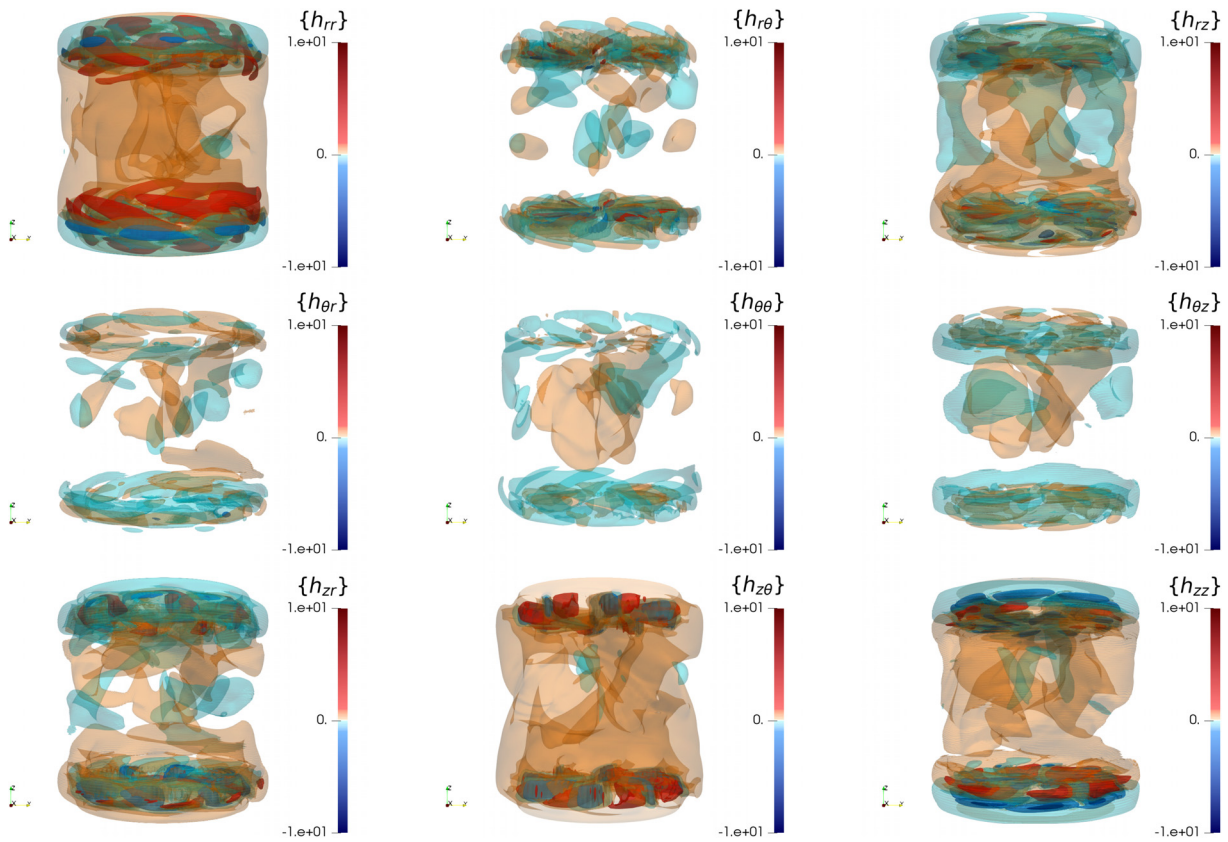| R_e	R_m	μ_r	R_m^c
1500	300	1	190 ± 10
1500	150	50	90 ± 5

FIG. 2. Time-averaged helicity tensor $\{h_{ij}\}$ in the saturated regime for $\mu_r = 50$.

minima are dispersed over the whole fluid domain. The maxima are associated with the swirling vortices attached to each blade and occupying part of the space between the blades. These vortices are thought to be a key ingredient of the dynamo mechanism.[9,34,35]

The maximum absolute non-dimensional value of around 10 for both magnetic permeability values corresponds to the $\{h_{rr}\}, \{h_{zz}\}$ components. These terms may be associated with an α-effect that would transform a poloidal field (b_r, b_z) into a toroidal field b_θ (first phase of the dynamo loop). To close the dynamo loop, we need the $\{h_{\theta\theta}\}$ term that would transform the toroidal field into the poloidal field (second phase). This would lead to an α^2 dynamo mechanism, e.g., $(b_r, b_z) \xrightarrow{\{h_{rr}\},\{h_{zz}\}} b_\theta \xrightarrow{\{h_{\theta\theta}\}} (b_r, b_z)$.

Another possibility to transform a poloidal field into a toroidal field (first phase of the dynamo loop) is to resort to Ω terms as seen in Eq. (13). This would lead to an $\Omega - \alpha$ dynamo mechanism, e.g., $(b_r, b_z) \xrightarrow{\{\Omega_r'\},\{\Omega_z'\}} b_\theta \xrightarrow{\{h_{\theta\theta}\}} (b_r, b_z)$. These averaged Ω-terms are shown in Fig. 4. Their large structures are invariant under the R_π symmetry [as expressed in Eq. (E4)]. They are similar for the two values of μ_r and their maximum absolute non-dimensional value is around 10^2.

These two dynamo mechanisms may be present in the VKS setup as it is underlined in Refs. 11, 19, and 20. Our results are not in contradiction with these explanations. However, as we now show, the local energy budget procedure allows for a much finer analysis of the dynamo mechanisms.

V. DYNAMO GROWTH MECHANISMS FROM LOCAL ENERGY BUDGETS

We now turn to the analysis of the local energy budgets and show how they can be applied to identify important dynamo mechanisms that are absent in the mean-field formulation adapted to statistically stationary problems. The filtering is computed at three different scales $\frac{\ell}{\eta} = (0, 1, 16)$. The case $\frac{\ell}{\eta} = 0$ is used to obtain the quantities involved in the exact energy budgets (see Sec. III C). The other two filtering scales are chosen so as to correspond to two important scales: (i) the Kolmogorov scale $\ell = \eta$ below which all computed fields are regular due to numerical approximation; (ii) an "inertial scale" $\ell = 16\eta$. These serve to identify the mechanisms at small and large scales, as well as two interesting limiting processes: (i) the "laminar dynamo" mechanism, obtained when the limit $\ell \to 0$ is taken before the limit $(\nu, 1/\mu_0\sigma_0) \to 0$ is taken. This corresponds to a dynamo that is dominated by the mechanisms at the regular scale, via classical chaotic scale separation of the magnetic field lines and diffusion; (ii) the "fast dynamo" mechanism, when the limit $(\nu, 1/\mu_0\sigma_0) \to 0$ is taken before the limit $\ell \to 0$ is reached. This corresponds to a dynamo driven by the roughness of the velocity field, where the magnetic field lines separate stochastically and magnetic dissipation is provided by fast reconnexions.[30]

In the following, we thus represent quantities involved in the exact energy budgets of Sec. III C only at the scale $\ell = 0$, while the
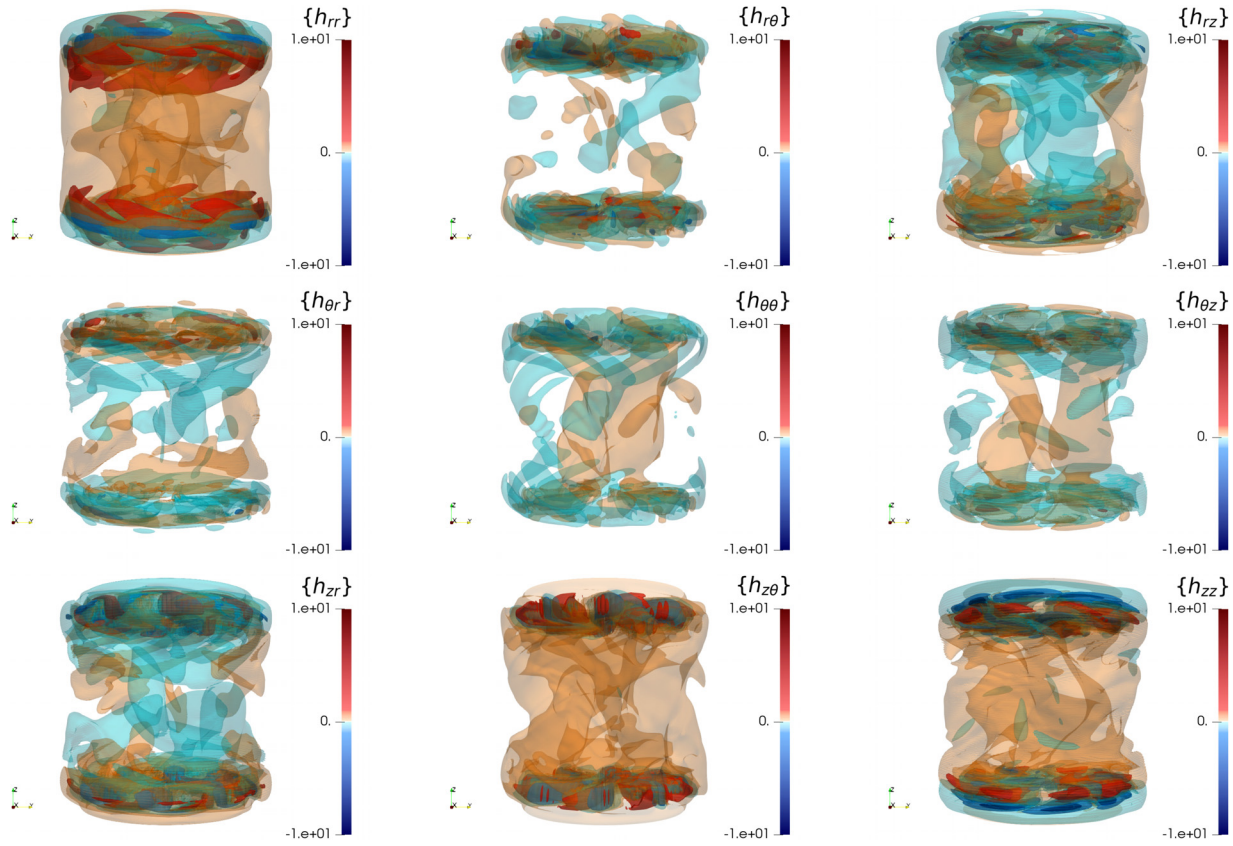
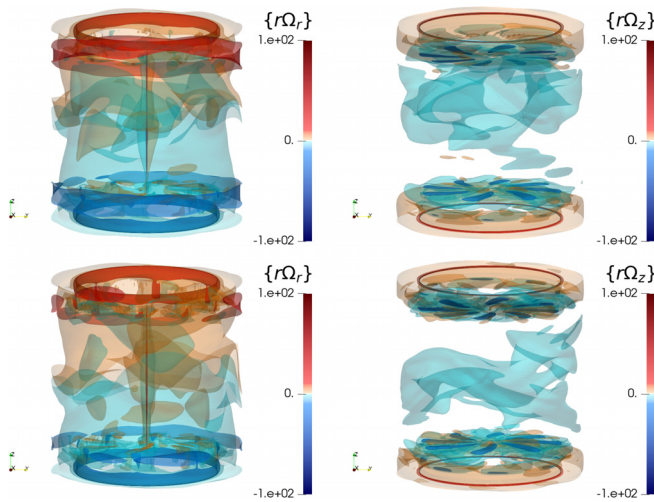**FIG. 3.** Time-averaged helicity tensor $\{h_{ij}\}$ in the saturated regime for $\mu_r = 1$.

FIG. 4. Time-averaged Ω effect in the saturated regime. Top row: $\mu_r = 50$, bottom row $\mu_r = 1$.

possibly irregular quantities are represented at $\frac{\ell}{\eta} = (1, 16)$ to highlight the laminar and fast dynamo mechanisms.

A. Time evolution of energy terms in the dynamo growth phase

Figure 5 shows that, in the growth regime of the dynamo, all transfer terms in the kinetic energy budget (19) are very similar for $\mu_r = 50$ and $\mu_r = 1$ and for each filtering scale. The reason is that the magnetic field is too weak to affect the velocity field. The only relevant terms are the viscous dissipation $\langle \mathcal{D}^\nu \rangle$ and the anomalous dissipation $\langle \mathcal{D}^u \rangle$ (for $\ell > 0$). $\langle \mathcal{D}^\nu \rangle$ decreases with ℓ as expected since viscosity acts on small scales. In contrast, $\langle \mathcal{D}^u \rangle$ increases with ℓ as a result of energy cascade from large to small scale, see Ref. 25.

Figure 6 shows the exponential growth in time (in absolute value) of all terms involved in the magnetic energy budget (20) for the two magnetic permeabilities. In order to better discriminate the respective role of these terms, we renormalize them on Fig. 7 by the space-averaged magnetic energy, $\langle E^m \rangle(t)$.

We can note that the two dynamo regimes are different. For $\mu_r = 1$ and $\ell = 0$, the growth rate is given by
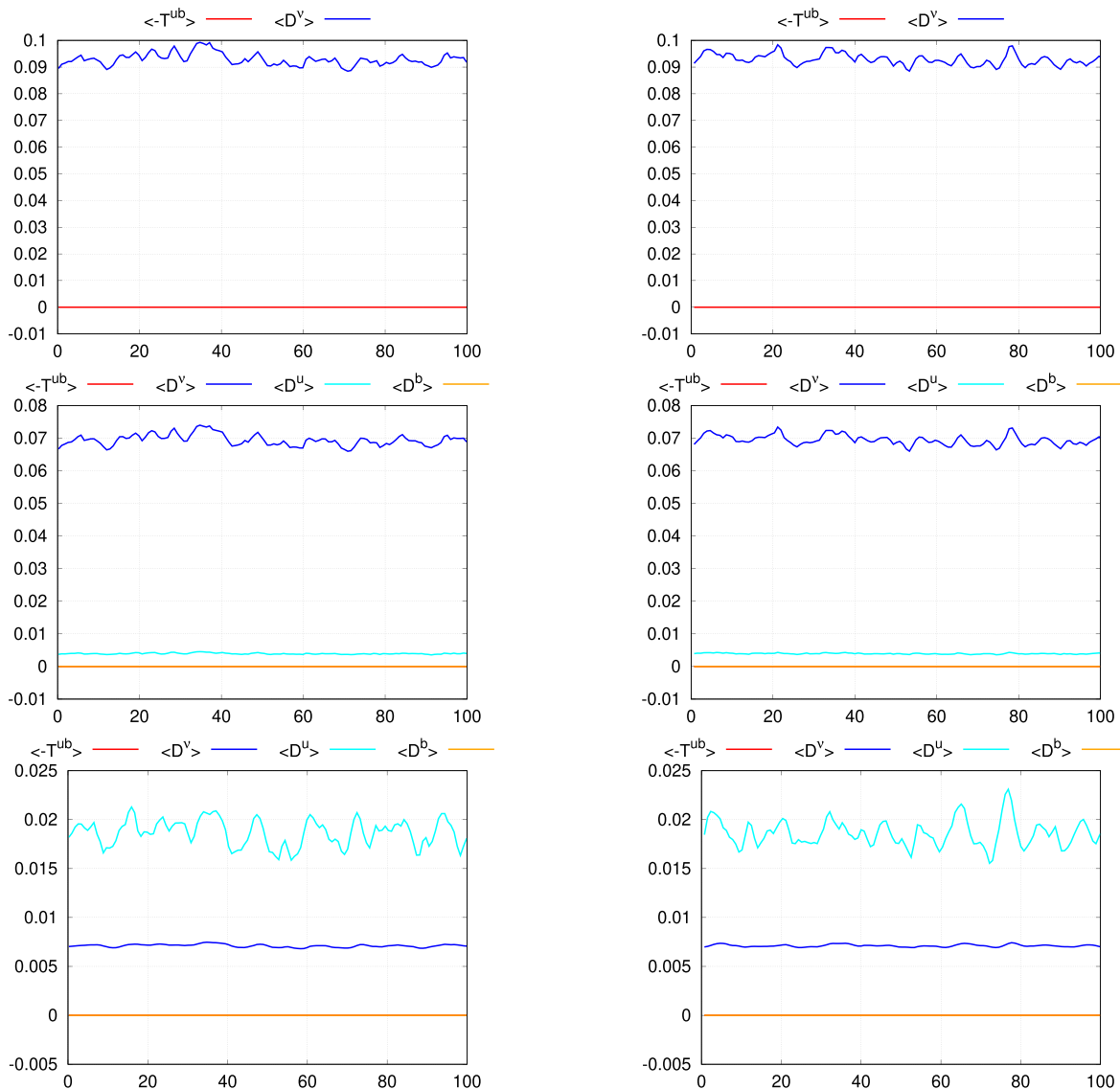
FIG. 5. Time evolution of kinetic energy budget (19) in the growing phase. Panels correspond to $\frac{\ell}{\eta} = 0$ for the first row, $\frac{\ell}{\eta} = 1$ for the second row, $\frac{\ell}{\eta} = 16$ for the third row, and the case $R_e = 1500$, $R_m = 150$, and $\mu_r = 50$ on the first column and the case $R_e = 1500$, $R_m = 300$, and $\mu_r = 1$ on the second column.

$$\langle \lambda_0^m \rangle = \frac{\langle \mathcal{T}_0^{u\rightarrow b} \rangle - \langle \mathcal{D}_0^\sigma \rangle}{\langle E^m \rangle}. \tag{44}$$

Therefore, $\langle \mathcal{T}_0^{u\rightarrow b} \rangle$ must exceed $\langle \mathcal{D}_0^\sigma \rangle$ for the magnetic field to grow. The situation is similar for $\mu_r = 1$, $\ell = \eta$ where the terms associated with irregularity such as $\langle \mathcal{D}^b \rangle$ and $\langle \mathcal{D}^{\overline{\sigma}} \rangle$ are quasi-zero due to the fact that the fields are somehow regular at this scale. Increasing ℓ enhances the irregular transfer term $\langle \mathcal{D}^b \rangle$ (which is positive) and diminishes $\langle \mathcal{T}^{u\rightarrow b} \rangle$ and $\langle \mathcal{D}^\sigma \rangle$ while $\langle \mathcal{D}^{\overline{\sigma}} \rangle$ stays negligible. This may be an indication that in the inviscid limit, the dynamo could be sustained by irregularities of the velocity field, so that a fast dynamo could be achieved. However, in the present moderate Reynolds

number regime, the dominant term is $\langle \mathcal{T}^{u\rightarrow b} \rangle$, which compensates for all dissipative terms.

For $\mu_r = 50$, the first instants ($t < 3$) show the same behavior as that for $\mu_r = 1$. This means that $\langle \mathcal{T}^{u\rightarrow b} \rangle$ is crucial in "launching" the dynamo process. After the launch is achieved, however, the dynamo trajectory becomes very different, as the rotating magnet effect $\langle \mathcal{M}^\mu \rangle$ takes over and maintains the dynamo action, while $\langle \mathcal{T}^{u\rightarrow b} \rangle$ is negative acting therefore like an anti-dynamo Lorentz force power. Increasing ℓ enhances the modulus of the irregular terms: $\langle \mathcal{D}^{\mu \mathcal{T}} \rangle$ relates the jump in μ and the electromotive field ($u \times b$) and is positive; $\langle \mathcal{D}^b \rangle$ follows the variations of $\langle \mathcal{T}^{u\rightarrow b} \rangle$ and is negative, *i.e.*, it is an inverse cascade for the energy transfer between scales for both the velocity and
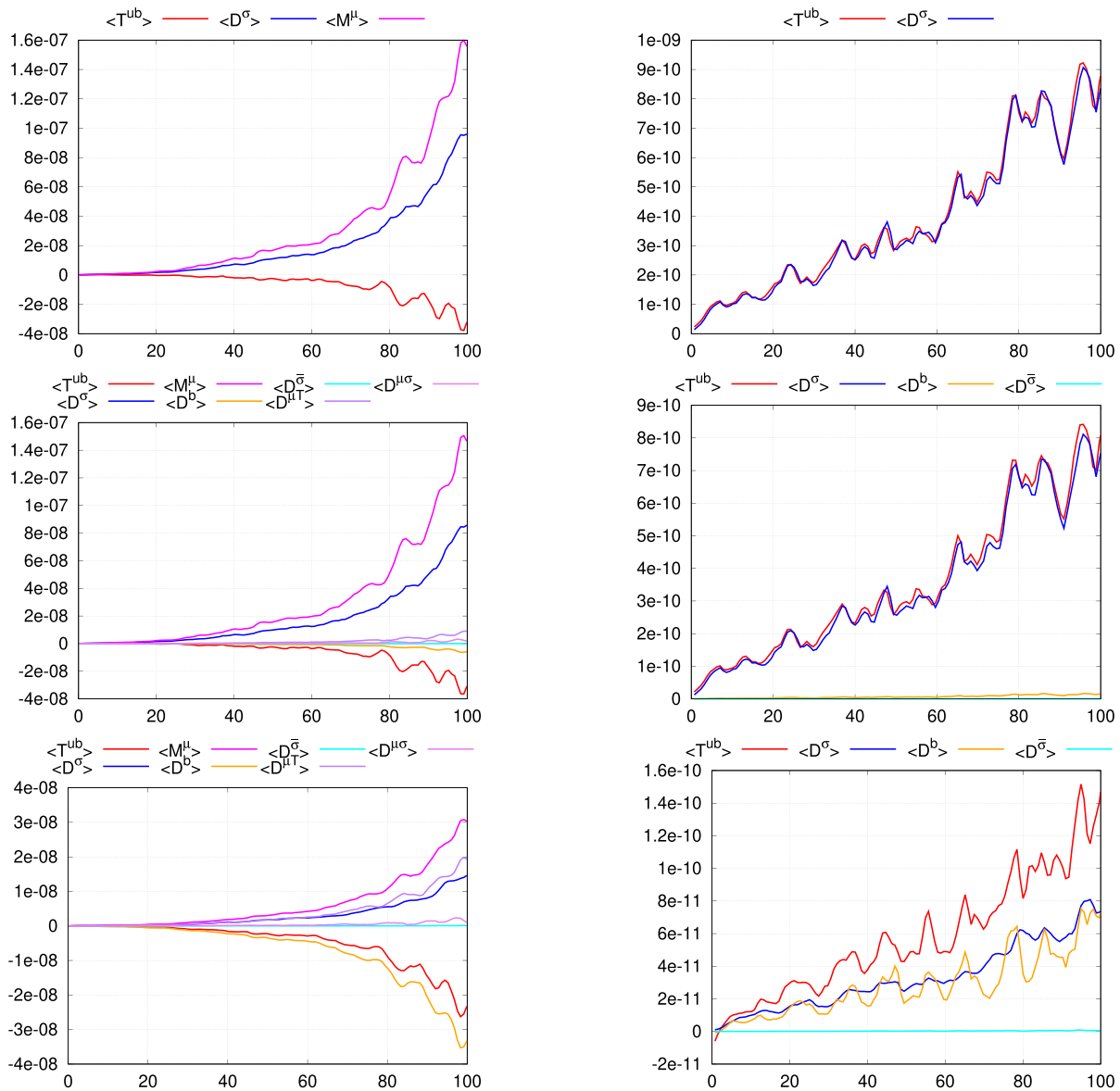
FIG. 6. Time evolution of magnetic energy budget (20) in the growing phase. Panels correspond to $\frac{\ell}{\eta} = 0$ for the first row, $\frac{\ell}{\eta} = 1$ for the second row, $\frac{\ell}{\eta} = 16$ for the third row, and the case $R_e = 1500$, $R_m = 150$, and $\mu_r = 50$ on the first column and the case $R_e = 1500$, $R_m = 300$, and $\mu_r = 1$ on the second column.

magnetic fields. The terms $\langle \mathcal{D}^{\mu\sigma} \rangle$ (correlation between the jump in μ and the current) and $\langle \mathcal{D}^{\bar\sigma} \rangle$ (dissipation due to the jump in σ) are negligible and can be ignored.

In summary, the term $\mathcal{T}^{u\to b}$ is essential to launch the dynamo in both cases, highlighting the crucial role played by the velocity field structure in the lightning of the dynamo. However, the further development of the dynamo is very different in the two cases, as $\mathcal{M}^{\mu}$ becomes the driving source term for the dynamo when using soft iron impellers, while $\mathcal{T}^{u\to b}$ becomes anti-dynamo. To further characterize these different mechanisms, we now consider the spatial localization of the local growth rate of the magnetic field.

B. Spatial distribution of linear growth rate

We use Eqs. (37) and (39) to determine the time-averaged local dynamo growth rate $\{\lambda^m\}$. The spatial distributions (Fig. 8) are different depending on the value of the magnetic permeability: for $\mu_r = 50$, the growth rate is localized near the impellers for each ℓ while, for $\mu_r = 1$, the main localizations are near the impellers and the shear-layer. In this region, the growth rate is positive inside the bulk and negative near the lateral wall at $r = 1$ for each ℓ. Therefore, the source of the growing magnetic field is very different depending on the impeller material.
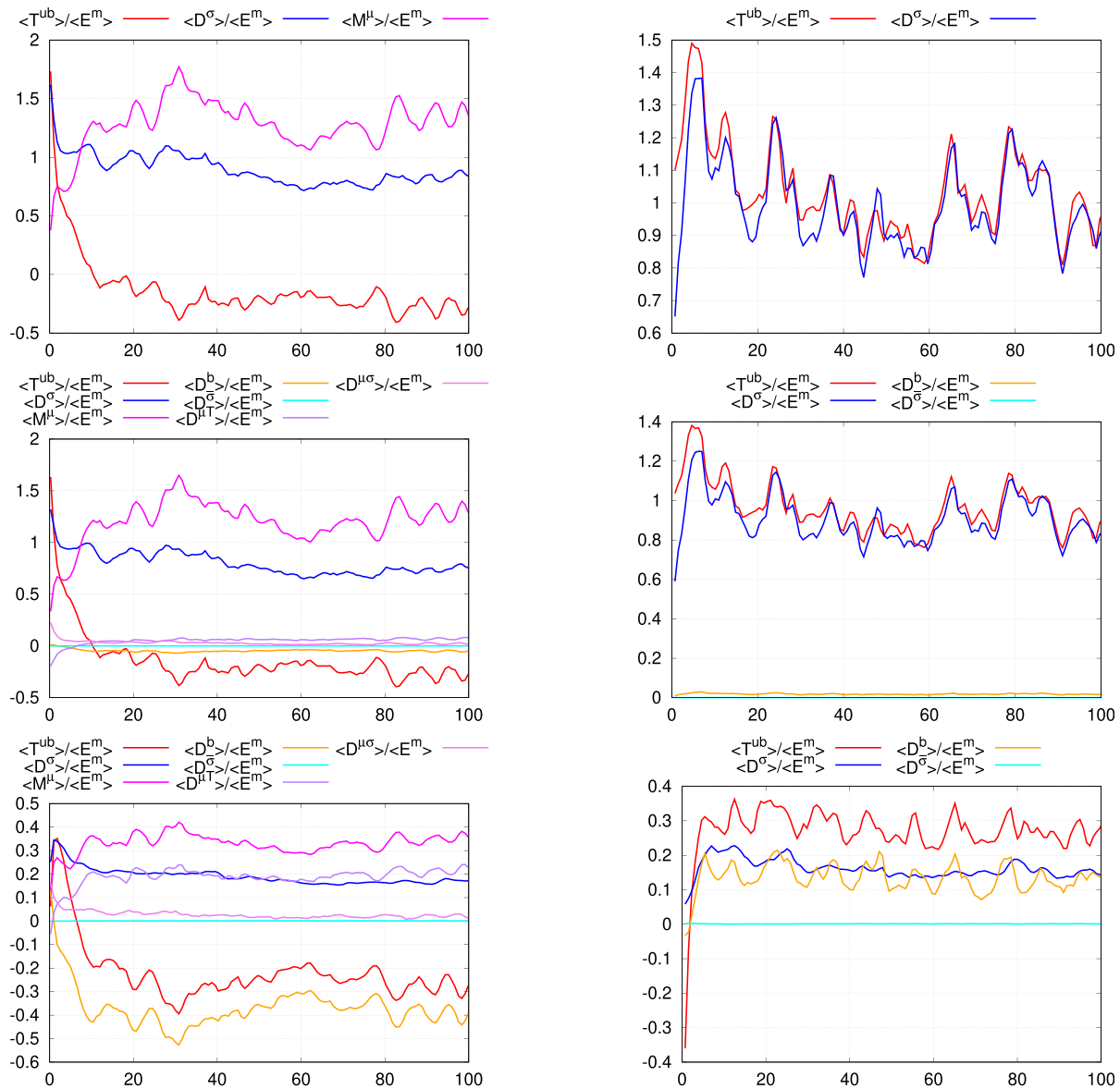
FIG. 7. Time evolution of renormalized magnetic budget in the growing phase. Panels correspond to $\frac{\ell}{\eta}=0$ for the first row, $\frac{\ell}{\eta}=1$ for the second row, $\frac{\ell}{\eta}=16$ for the third row, and the case $R_e=1500$, $R_m=150$, and $\mu_r=50$ on the first column and the case $R_e=1500$, $R_m=300$, and $\mu_r=1$ on the second column.

C. Local energy transfers between scales in the growth regime

The anomalous dissipation (Fig. 9) $\{\mathcal{D}^u\}$ is similar for both permeabilities at each scale ℓ in the growth stage. At $\ell=0$, it reaches the zero machine as expected and is thus not shown. For $\ell=\eta$ and $\ell=16\eta$, it is mainly positive in the bulk where large scales provide energy to small scales and it is negative near the impellers where small scales feed large scales through the motion of the impellers blades. This behavior highlights the energy cascade at work in the von Kármán flow, where energy is injected at the blades, and transferred toward smaller scales in the bulk of the flow.

In contrast, the anomalous magnetic dissipation $\{\mathcal{D}^b/\langle E^m\rangle\}$ (Fig. 10) is very different for both permeabilities. For $\mu_r=50$, for all ℓ, it is localized near the impellers and it becomes more negative when ℓ increases. Its spatial average is negative in this case as shown in Fig. 7 (left) which makes it an inverse energy cascade.

For $\mu_r=1$, blobs of alternate signs are localized near the impellers while larger areas of positive $\{\mathcal{D}^b/\langle E^m\rangle\}$ are localized around the shear layer. The fact that $\{\mathcal{D}^b/\langle E^m\rangle\}$ is negative (pro-dynamo sign) near the impellers and not in the shear-layer is in agreement with the mean-field arguments based on helicity.[9]
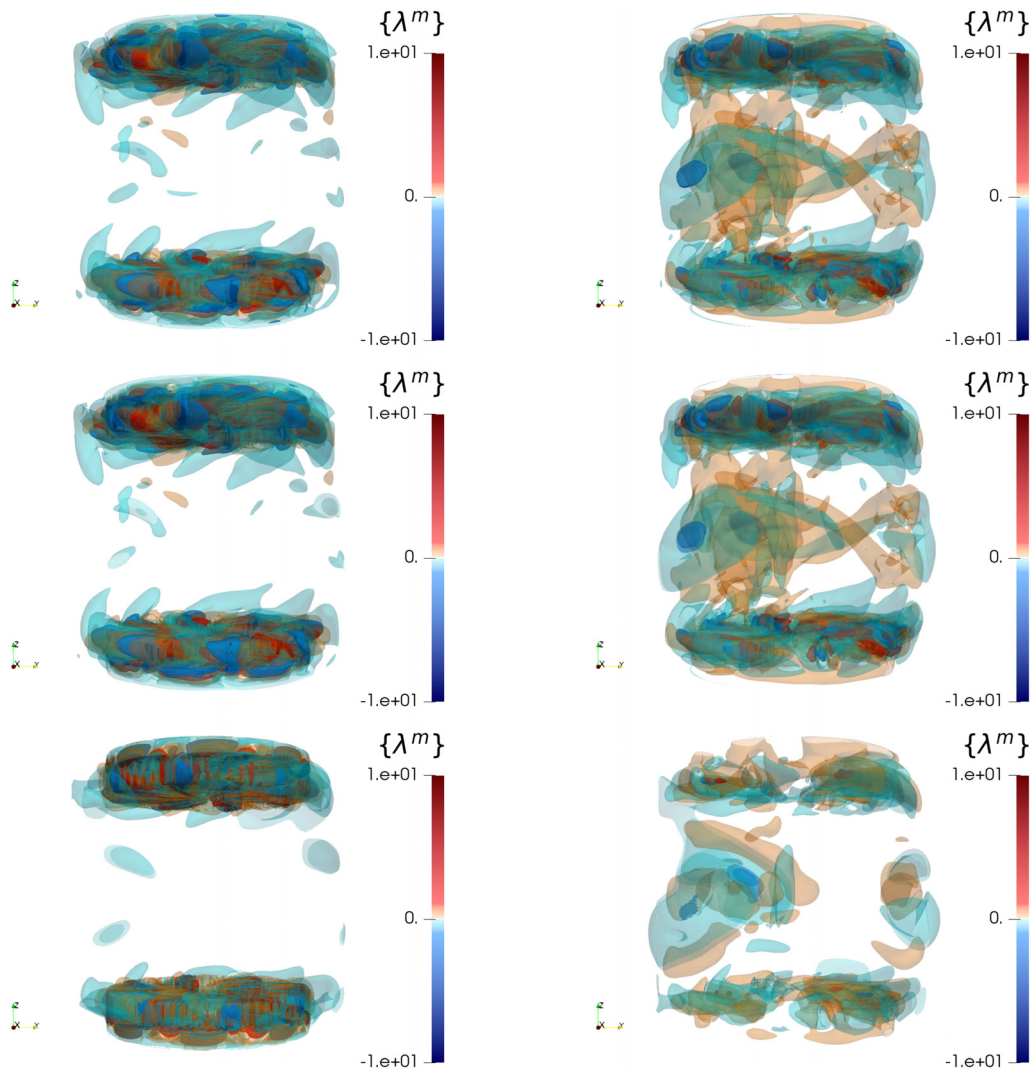
FIG. 8. Dynamo growth rate averaged on the 128 snapshots in the dynamo growth regime. Panels correspond to $\frac{\ell}{\eta} = 0$ for the first row, $\frac{\ell}{\eta} = 1$ for the second row, $\frac{\ell}{\eta} = 16$ for the third row, and the case $R_e = 1500$, $R_m = 150$, and $\mu_r = 50$ on the first column and the case $R_e = 1500$, $R_m = 300$, and $\mu_r = 1$ on the second column.

D. Conversion of energy in the growth regime

We now examine the two source terms already identified. As they do not vary much with the scale only the case $\ell = 0$ is discussed. At the early stage $t < 3$, the (minus) power of the Lorentz force (Fig. 7) $\langle \mathcal{T}^{u \to b} \rangle / \langle E^m \rangle$ is positive for both permeabilities, but beyond, its sign and spatial repartition are very different depending on the value of μ_r as seen on Fig. 11.

For $\mu_r = 1$, $\{ \mathcal{T}^{u \to b} / \langle E^m \rangle \}$ shows alternated signed zones near the impellers and positive areas in the bulk. The latter contributes to a positive space average, which is compatible with the standard dynamo mechanisms linked with the presence of differential rotation and vortices in the shear layer and within the disks.

For $\mu_r = 50$, we can observe two behaviors: at sufficiently small scales, it is positive within the shear layer, showing that the kinetic dynamo mechanism is still present. However, this mechanism is

countered by an anti-dynamo mechanism occurring near the impellers, where the term alternates sign such that its spatial average is negative. Another term is required for the dynamo to be sustained: the rotating magnet effect $\{ \mathcal{M}^u / \langle E^m \rangle \}$. As shown in Fig. 12 at $\ell = 0$, this magnet term is also only localized in the blades and disks with alternate signs, its averaged contribution being positive.

VI. SATURATION OF THE DYNAMO FROM LOCAL ENERGY BUDGETS

To determine the main mechanisms for dynamo saturation (when $\partial_t \langle E^c \rangle = 0$ and $\partial_t \langle E^m \rangle = 0$ on average), we now consider the local energy budget given by (19)–(20) and evaluate the spatial average of all its components as a function of time. We want to determine what is the dominant balance. We next describe the spatial distribution
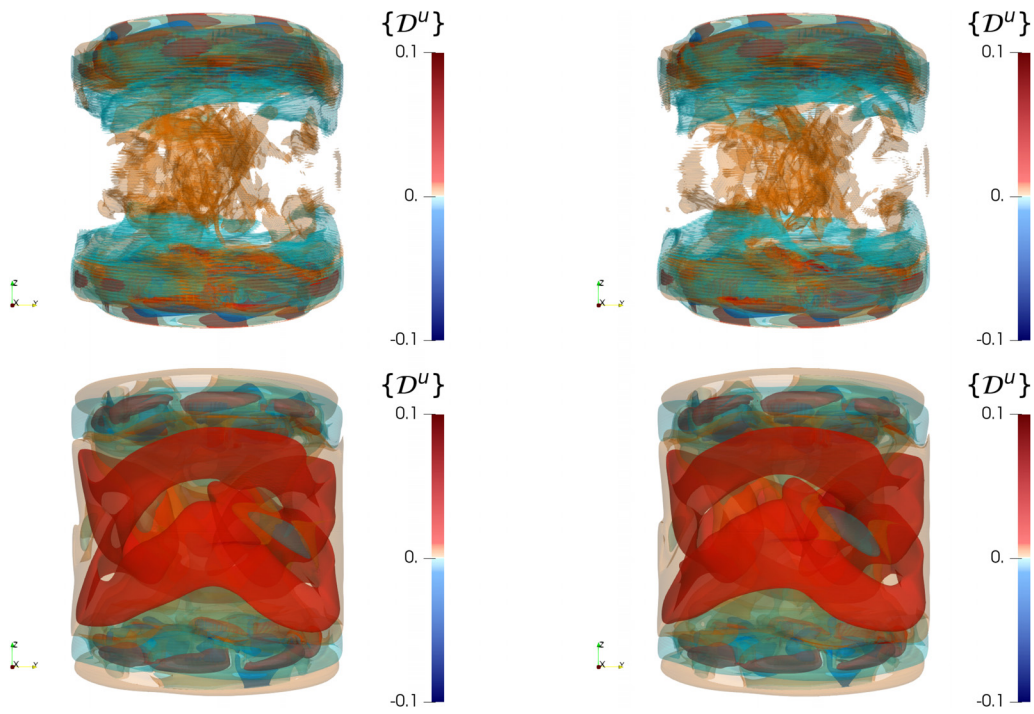
27 February 2024 16:13:02

FIG. 9. Time-averaged anomalous velocity dissipation in the growth regime. Panels correspond to $\frac{\ell}{\eta} = 1$ for the first row, $\frac{\ell}{\eta} = 16$ for the second row, and the case $R_e = 1500$, $R_m = 150$, and $\mu_r = 50$ on the first column and the case $R_e = 1500$, $R_m = 300$, and $\mu_r = 1$ on the second column.
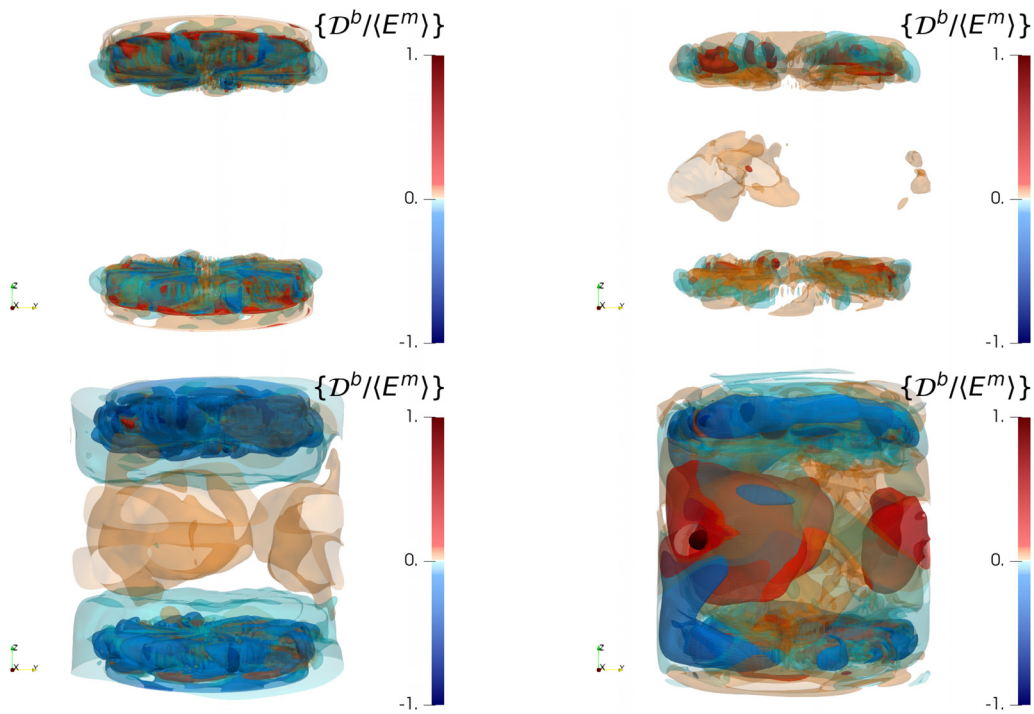

FIG. 10. Renormalized and time-averaged anomalous magnetic dissipation in the growth regime. Panels correspond to $\frac{\ell}{\eta} = 1$ for the first row, $\frac{\ell}{\eta} = 16$ for the second row, and the case $R_e = 1500$, $R_m = 150$, and $\mu_r = 50$ on the first column and the case $R_e = 1500$, $R_m = 300$, and $\mu_r = 1$ on the second column.
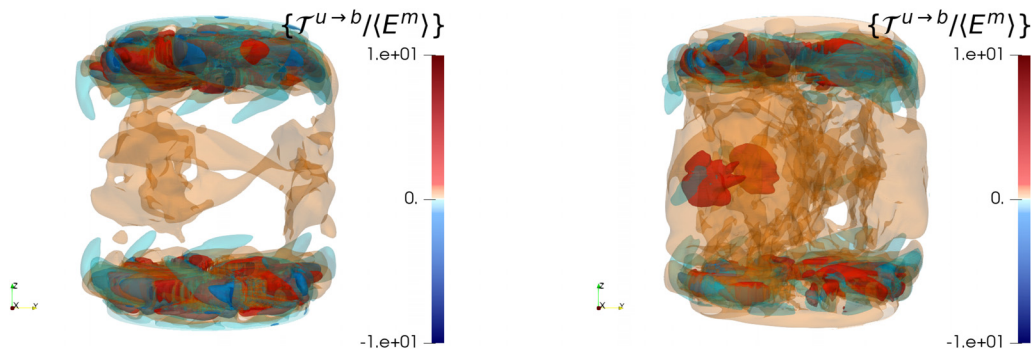
FIG. 11. Renormalized and time-averaged energy transfer between fields in the growth regime at $\ell = 0$. Left panel: $R_e = 1500$, $R_m = 150$, and $\mu_r = 50$. Right panel: $R_e = 1500$, $R_m = 300$, and $\mu_r = 1$.

of each term of the energy budget averaged on a time range belonging to the saturated regime for the two types of dynamo action.

A. Time evolution of energy terms in the dynamo saturated phase

Concerning the kinetic energy budget displayed in Fig. 13, for $\mu_r = 1$, $\langle \mathcal{D}^\nu \rangle$ and $\langle \mathcal{D}^u \rangle$ follow the same behavior as in the growth regime displayed in Fig. 5: $\langle \mathcal{D}^\nu \rangle$ is positive and decreases with ℓ, $\langle \mathcal{D}^u \rangle$ is positive and increases with ℓ. The transfer from the velocity field to the magnetic field is strong enough to be shown by the term $-\langle \mathcal{T}^{u \to b} \rangle$, which is negative for all filtering scales. The irregular term $\langle \mathcal{D}^b \rangle$ is positive and acts as a direct energy cascade. Consequently, the velocity field maintains the magnetic field via the $-\langle \mathcal{T}^{u \to b} \rangle$ term and against all dissipative terms.

In contrast, for $\mu_r = 50$ in the saturated regime, the term $-\langle \mathcal{T}^{u \to b} \rangle$ is positive and $\langle \mathcal{D}^b \rangle$ is negative. Hence, $-\langle \mathcal{T}^{u \to b} \rangle$ is a source term for the velocity field which extracts energy from the magnetic field and $\langle \mathcal{D}^b \rangle$ is an inverse cascade. The other terms, $\langle \mathcal{D}^\nu \rangle$, $\langle \mathcal{D}^u \rangle$, are positive and behave like in the case $\mu_r = 1$.

Concerning the magnetic balance displayed in Fig. 14, the time evolution of $\langle \mathcal{T}^{u \to b} \rangle$, $\langle \mathcal{D}^\sigma \rangle$, $\langle \mathcal{D}^b \rangle$ and $\langle \mathcal{D}^{\overline{\sigma}} \rangle$ for $\mu_r = 1$ is similar to the
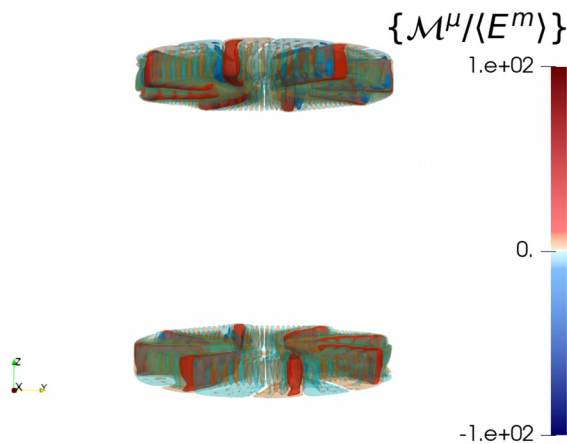

FIG. 12. Renormalized and time-averaged rotating magnet effect for the case $R_e = 1500$, $R_m = 150$, $\mu_r = 50$ at $\ell = 0$ in the growth regime.

one of the renormalized terms $\langle \mathcal{T}^{u \to b} \rangle / \langle E^m \rangle$, $\langle \mathcal{D}^\sigma \rangle / \langle E^m \rangle$, $\langle \mathcal{D}^b \rangle / \langle E^m \rangle$ and $\langle \mathcal{D}^{\overline{\sigma}} \rangle / \langle E^m \rangle$ shown in Fig. 7 (right column) except for the time interval $[970 : 990]$. In this interval, $\langle \mathcal{T}^{u \to b} \rangle - \langle \mathcal{D}^b \rangle - \langle \mathcal{D}^\sigma \rangle$ is negative and the magnetic energy decreases locally in time. Anyway, $\langle \partial_t E^m \rangle$ is statistically around 0.

For $\mu_r = 50$, the time evolution of all terms of Eq. (20) follows that of the renormalized terms $\langle \mathcal{M}^\mu \rangle / \langle E^m \rangle$, $\langle \mathcal{T}^{u \to b} \rangle / \langle E^m \rangle$, $\langle \mathcal{D}^{\mu\sigma} \rangle / \langle E^m \rangle$, $\langle \mathcal{D}^b \rangle / \langle E^m \rangle$, $\langle \mathcal{D}^{\mu T} \rangle / \langle E^m \rangle$ of Fig. 7 (left column) with $\langle \mathcal{D}^{\mu T} \rangle$ larger than $\langle \mathcal{D}^\sigma \rangle$. The terms $\langle \mathcal{D}^{\overline{\sigma}} \rangle$ and $\langle \mathcal{D}^{\mu\sigma} \rangle$ are negligible. The positive term $\langle \mathcal{M}^\mu \rangle - \langle \mathcal{D}^b \rangle$ compensates the negative term $\langle \mathcal{T}^{u \to b} \rangle - \langle \mathcal{D}^\sigma \rangle - \langle \mathcal{D}^{\mu T} \rangle$ for the magnetic field to be maintained.

B. Kinetic and magnetic energy repartition

In the saturated dynamo regime, we can study the spatial distribution of the statistically stationary energies. The kinetic energy is a regular field represented at $\ell = 0$ in Fig. 15. For both μ_r cases, it is mainly localized near the impellers as expected. However, it presents more fine structures in the bulk for the $\mu_r = 1$ case than for the $\mu_r = 50$ case.

In contrast, the magnetic energy (Fig. 16) shows very different shapes depending on the relative magnetic permeability. For high μ_r, it is concentrated near the impellers and is mainly axisymmetric. In contrast, at $\mu_r = 1$, the magnetic energy spreads across the entire volume and presents non-axisymmetric features. These results are coherent with the dominant axisymmetric Fourier mode $m_F = 0$ for the magnetic field at $\mu_r = 50$ and the mixing of $m_F = 0, 1$ magnetic modes at $\mu_r = 1$ as indicated in Table III of Ref. 21

C. Local energy transfers between scales

The most interesting feature of the filtering process is to highlight the energy transfer that happens in-between different scales via the $\mathcal{D}^u$ and $\mathcal{D}^b$ terms. These terms vanish in the limit $\ell \to 0$ in our simulation, but they may provide finite contributions for sufficiently rough velocity fields, resulting in anomalous dissipation and fast dynamo mechanism.[22,23]

Figure 17 displays $\{\mathcal{D}^u\}$. This term has only a kinetic origin linked to the Navier–Stokes equations.[27] In the inviscid limit, it may contribute to the non-vanishing dissipation observed in the von Kármán flow.[32,36] For $\ell = \eta$, it is mainly localized near the impellers. For $\ell = 16\eta$, more positive and negative regions appear. The negative
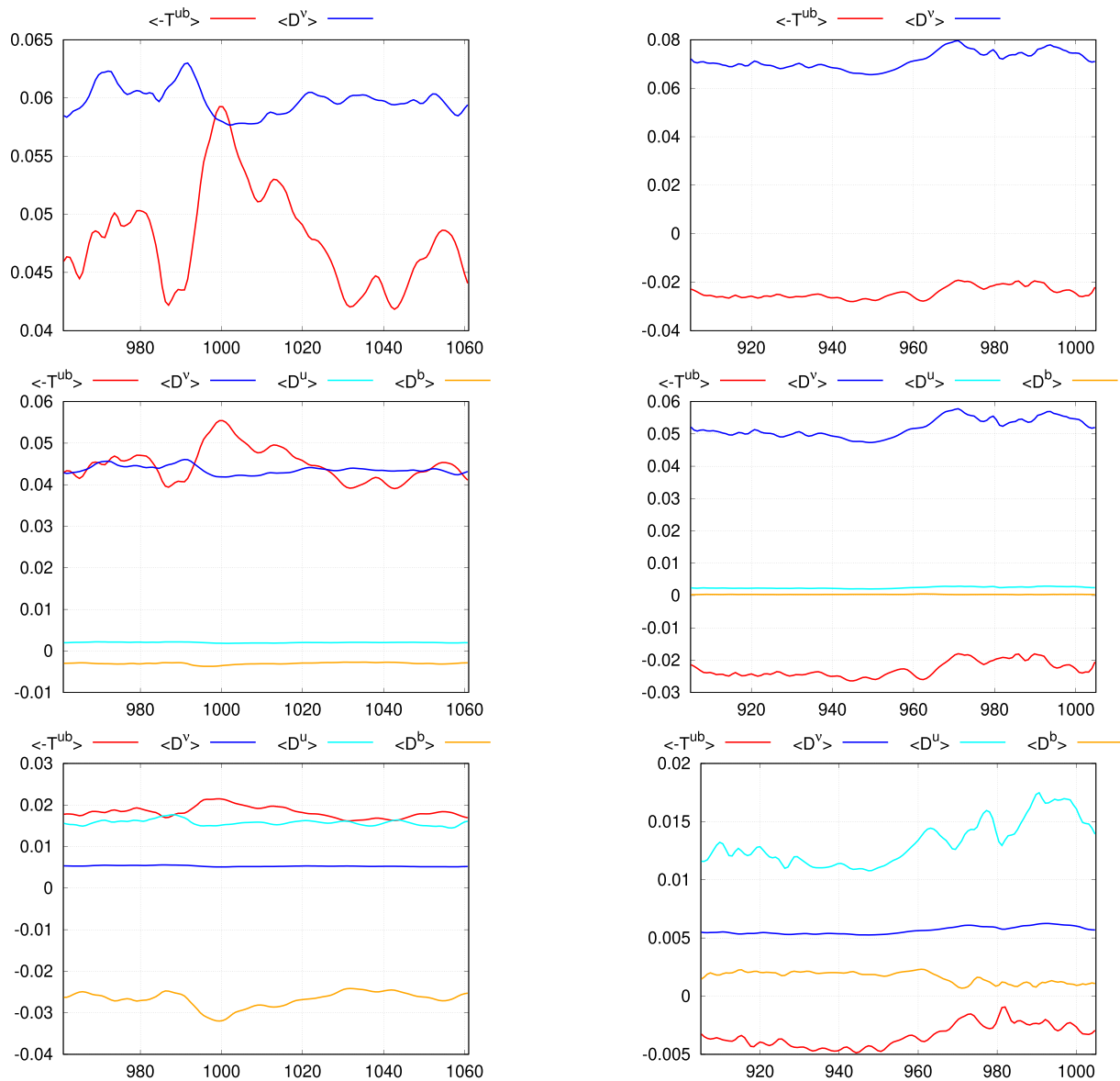
FIG. 13. Time evolution of kinetic energy budget (19) in the saturated phase. Panels correspond to $\frac{\ell}{\eta} = 0$ for the first row, $\frac{\ell}{\eta} = 1$ for the second row, $\frac{\ell}{\eta} = 16$ for the third row, and the case $R_e = 1500$, $R_m = 150$, and $\mu_r = 50$ on the first column and the case $R_e = 1500$, $R_m = 300$, and $\mu_r = 1$ on the second column.

ones correspond to areas where the scales smaller than 16η inject energy into the system. They are found near the impellers but also near the lateral wall, highlighting the non-homogeneity of the cascade and the importance of the boundaries in the transfer mechanism.

Due to the presence of the magnetic induction, a new transfer channel is expected allowing transfers from kinetic to magnetic energy through the term $\{\mathcal{D}^b\}$, that can provide a fast dynamo mechanism in the inviscid limit,[29] for rough enough velocity fields. As seen in Fig. 18, this term is dominantly localized near the impellers for $\mu_r = 50$.

Patterns with alternate signs are stuck to the blades but their spatial average is negative as shown in Fig. 14 (bottom left column panel). That means that an inverse cascade involving the velocity and magnetic fields exists from small scales to large scales near the impellers.

Similarly, for $\mu_r = 1$, spots of alternate signs are close to the impellers, but complex positive structures also form close to the shear layer as ℓ increases. These positive regions are dominant and contribute to an overall positive spatial average, as shown in Fig. 14 (bottom right column panel). In this case, the cascade involving the velocity and magnetic fields is direct from large scales to small scales.
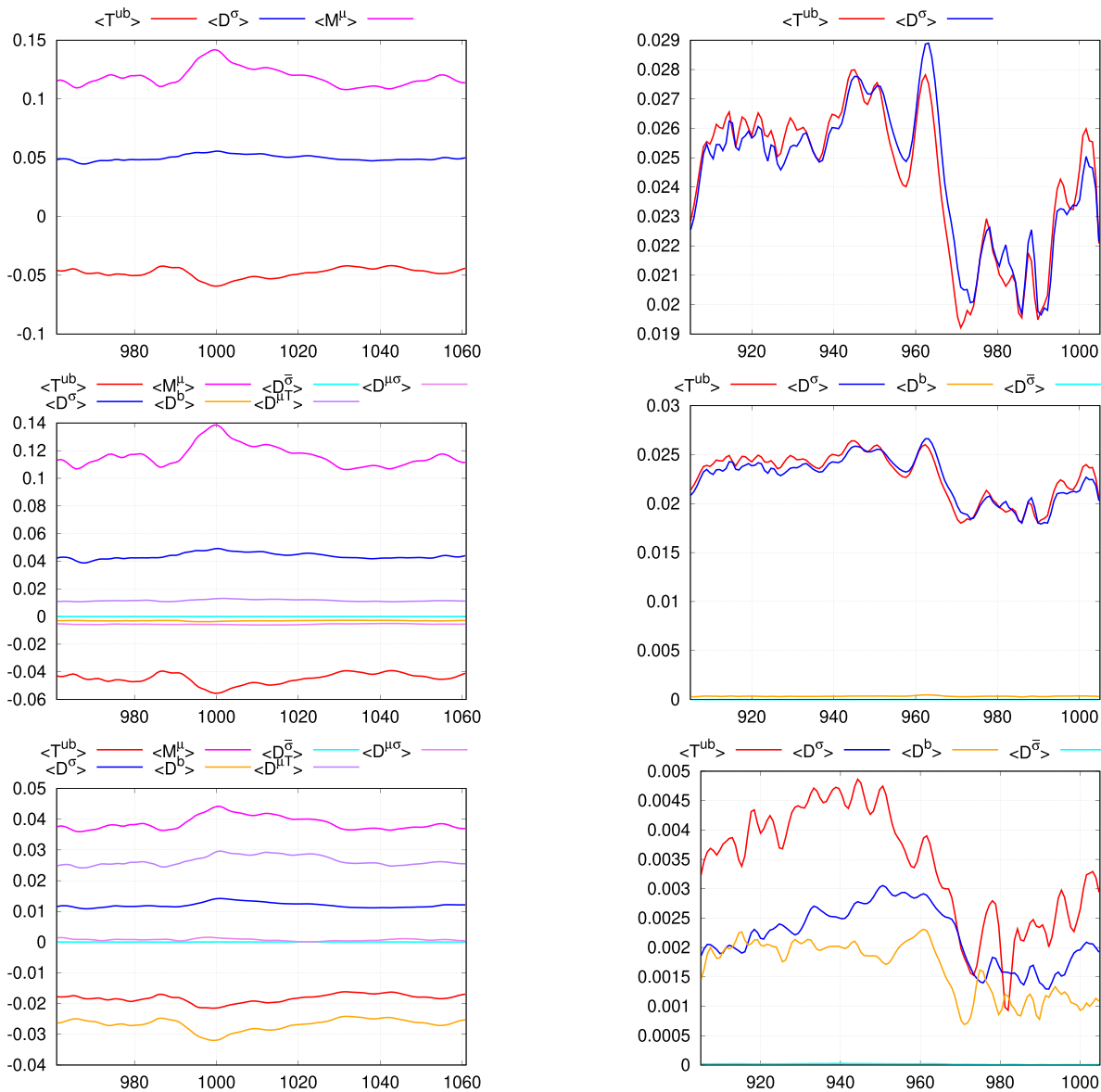
FIG. 14. Time evolution of magnetic energy budget (20) in the saturated phase. Panels correspond to $\frac{\ell}{\eta} = 0$ for the first row, $\frac{\ell}{\eta} = 1$ for the second row, $\frac{\ell}{\eta} = 16$ for the third row, and the case $R_e = 1500$, $R_m = 150$, and $\mu_r = 50$ on the first column and the case $R_e = 1500$, $R_m = 300$, and $\mu_r = 1$ on the second column.

D. Conversion of energy

The conversion of kinetic energy to magnetic energy relies on the $\mathcal{T}^{u \to b}$ and $\mathcal{M}^{\mu}$ terms [as seen in Eq. (20)]. The former is the standard source term: when it is on average positive, the velocity field provides energy to the magnetic field; the opposite occurs when it is negative.

Figure 19 shows that the spatial variation of $\{\mathcal{T}^{u \to b}\}$ depends on the value of μ_r. For $\mu_r = 50$, it is localized near the impellers with alternate signs. Its spatial average is negative in the saturated regime as shown in Fig. 14 (left column). It corresponds to a loss of magnetic energy. For $\mu_r = 1$, there are more transfers in the bulk and smaller values in the impellers. Note that it is the only source term for the

maintenance of a magnetic field when $\mu_r = 1$. Therefore, it has to be positive on average for a magnetic field to saturate as it is seen in Fig. 14 (right column).

In contrast, for $\mu_r = 50$, $\{\mathcal{M}^{\mu}\}$ is another source of magnetic field increase. As shown in Fig. 20 at $\ell = 0$ this term only exists where the blades rotate as expected, and it clearly follows the azimuthal variation of the blades with $m_F = 8$. It is on average positive and greater than the negative average of $\{\mathcal{T}^{u \to b}\}$ (see Fig. 14 left column). This allows qualifying this dynamo as a magnet effect in the saturated regime. However, at the beginning of the linear regime, it is dominated by the $\{\mathcal{T}^{u \to b}\}$ term as shown in Fig. 7 for $t < 3$.
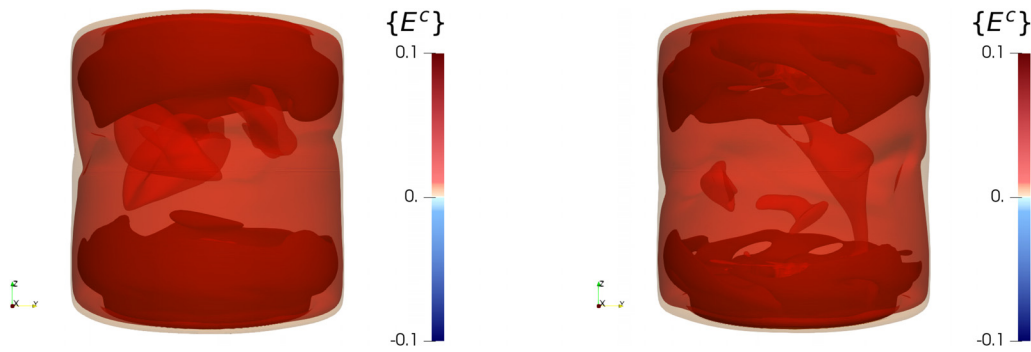
FIG. 15. Kinetic energy averaged on the 128 snapshots in the dynamo saturated regime at $\ell = 0$. Left panel: $R_e = 1500$, $R_m = 150$, and $\mu_r = 50$. Right panel: $R_e = 1500$, $R_m = 300$, and $\mu_r = 1$.

E. Dissipation and energy transfer through variation of magnetic permeability and electric conductivity

The variation of μ_r due to the impellers is responsible for the terms $\{\mathcal{D}^{\mu\sigma}\}$ and $\{\mathcal{D}^{\mu\mathcal{T}}\}$ as shown in Figs. 21 and 22. These are localized at the surface of the blades and disks. They exist only for $\ell > 0$ and show alternate signs. They are specific energy transfers between scales linked to jumps in magnetic permeability. The first one is induced by the Joule dissipation while the second one is induced by the Lorentz force power.

Figure 23 shows the Joule dissipation due to the irregularity of the electrical conductivity. As expected, it is located on the lateral border $\{r = 1.4, \ 0 \le \theta < 2\pi, -1 \le z \le 1\}$ where the conductivity has a jump from the stagnant liquid sodium layer to the copper vessel. For all filter scales, it remains low (maximum absolute values around 10^{-4}) and is, therefore, not really relevant to the dynamo action.

VII. MECHANISMS FOR DYNAMO ACTION

Inspection of the linear regime has proved that the standard mechanism for the growth of the dynamo acts for both values of the impellers permeability at early instants: as soon as the threshold in magnetic Reynolds number is exceeded, the (minus) Lorentz force power overrides the dissipative terms. For steel impellers ($\mu_r = 1$), at larger times, a balance between $\mathcal{T}^{u \to b}$ (which is in space-average positive) and the dissipative terms (whose space-average values are

positive) is reached and allows a saturated regime to be achieved. In contrast, for soft iron impellers ($\mu_r = 50$), the rotating magnet effect due to the motion of μ_r and the anomalous magnetic dissipation (which is negative on space-average) take over and become the key players for the dynamo mechanism in the saturation phase. In light of our findings, we can now discuss the different scenarios proposed in the literature to explain the VKS dynamo.

The mechanism based upon spatial variations in electrical conductivity was first proposed by Busse and Wicht.[12] These authors have considered the magnetic field generation by an electrically conducting fluid flowing parallel to a rigid plate presenting spatial variations of electrical conductivity in the streamwise direction. It was shown that the magnetic Reynolds number for the dynamo process decreases with increasing conductivity of the plate and with increasing amplitude of its modulation. The growth mechanism is the coupling between poloidal and toroidal components of the magnetic field through the high conductivity zones. This mechanism was also recovered in Refs. 13 and 14. In Ref. 37, a Bullard-type homopolar disk dynamo is experimentally realized using a copper disk positioned co-axially beneath a flat, multi-arm spiral coil of the same size and electrically coupled to it along the perimeter and at the center by Galinstan contacts. The spiral grooves create an axial magnetic field by deflecting the coil's current in an azimuthal manner, making the dynamo essentially axisymmetric. Therefore, the dynamo mechanism relies largely on the anisotropic geometry of the coil, which forces the current to follow deflected paths.
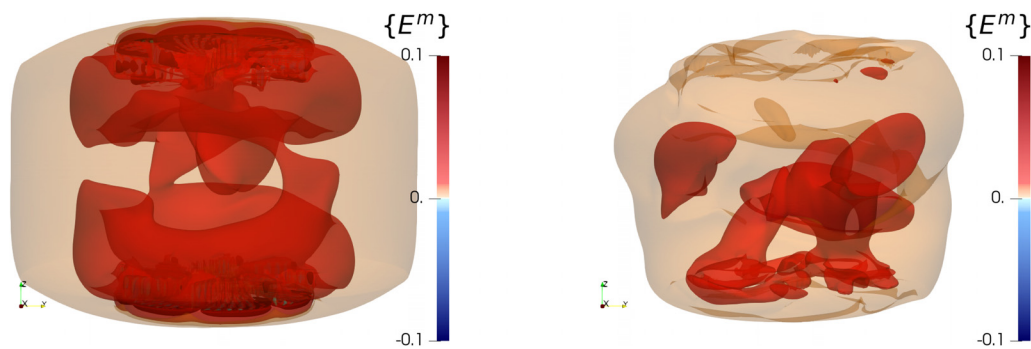

FIG. 16. Time-averaged magnetic energy in the saturated regime at $\ell = 0$. Left panel: $R_e = 1500$, $R_m = 150$, and $\mu_r = 50$. Right panel: $R_e = 1500$, $R_m = 300$, and $\mu_r = 1$.
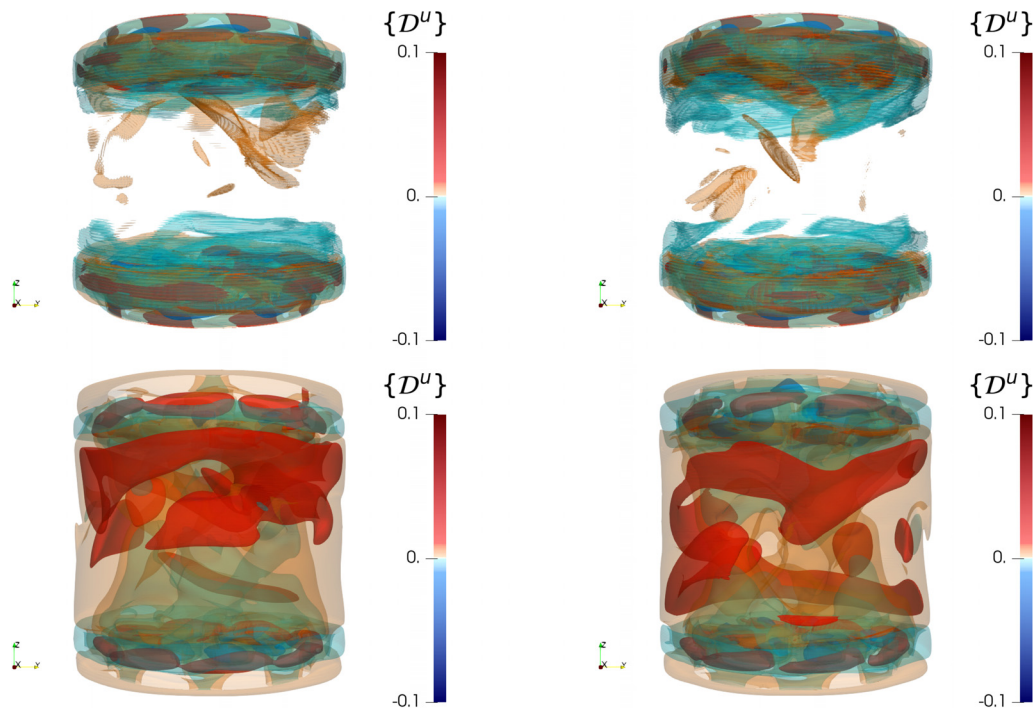
FIG. 17. Time-averaged anomalous velocity dissipation in the saturated regime. Panels correspond to $\frac{\ell}{\eta} = 1$ for the first row, $\frac{\ell}{\eta} = 16$ for the second row, and the case $R_e = 1500$, $R_m = 150$, and $\mu_r = 50$ on the first column and the case $R_e = 1500$, $R_m = 300$, and $\mu_r = 1$ on the second column.

FIG. 18. Time-averaged anomalous magnetic dissipation in the saturated regime. Panels correspond to $\frac{\ell}{\eta} = 1$ for the first row, $\frac{\ell}{\eta} = 16$ for the second row, and the case $R_e = 1500$, $R_m = 150$, and $\mu_r = 50$ on the first column and the case $R_e = 1500$, $R_m = 300$, and $\mu_r = 1$ on the second column.
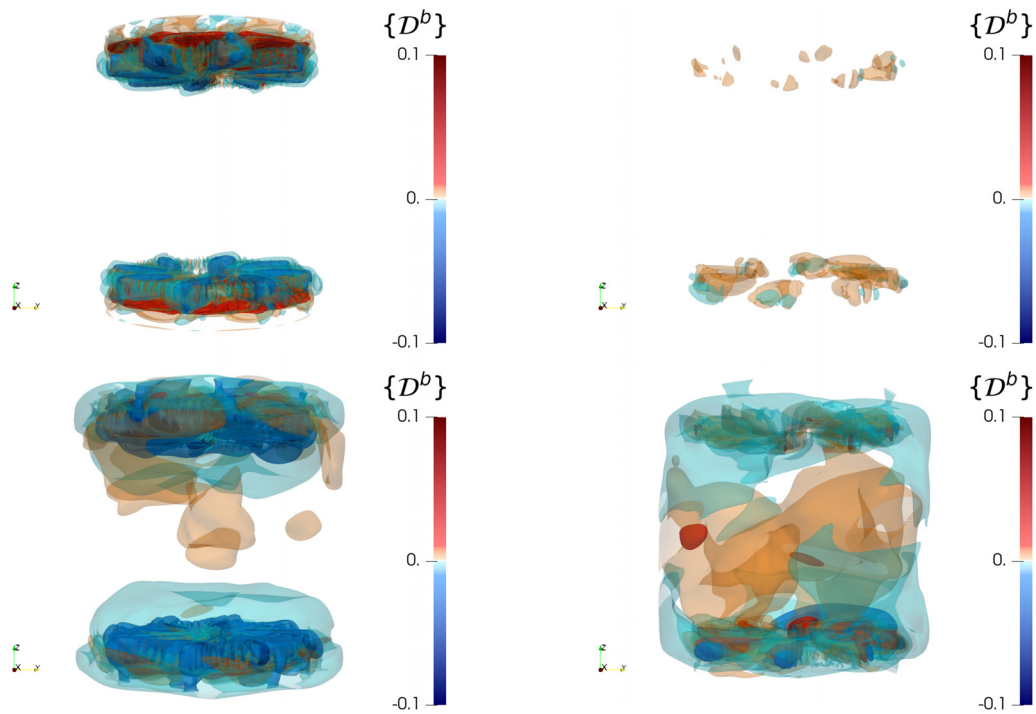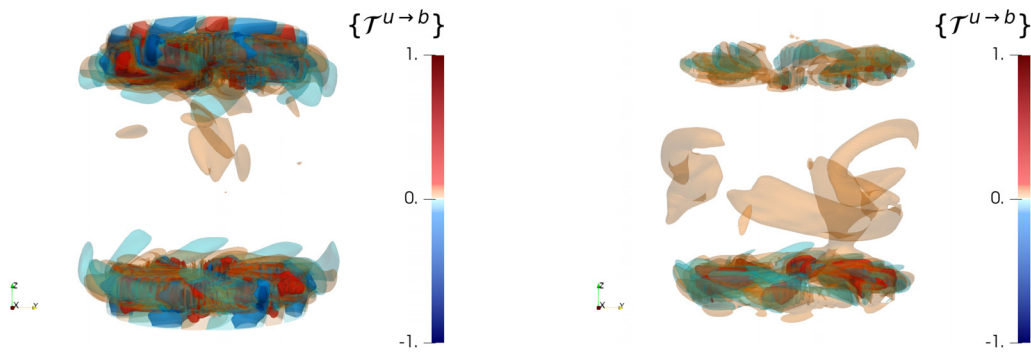
FIG. 19. Time-averaged energy transfer between fields in the saturated regime at $\ell = 0$. Left panel: $R_e = 1500$, $R_m = 150$, and $\mu_r = 50$. Right panel: $R_e = 1500$, $R_m = 300$, and $\mu_r = 1$.
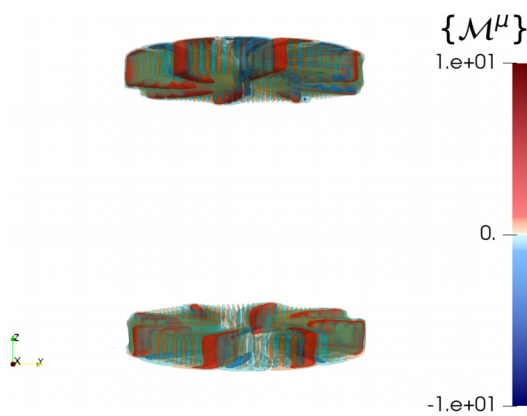

FIG. 20. Time-averaged rotating magnet effect for the case $R_e = 1500$, $R_m = 150$, $\mu_r = 50$ in the saturated regime at $\ell = 0$.

The same mechanism is at work in the Fury experiment[38] where a copper rotor with grooves rotates inside a copper grooved stator, electrically connected with a thin layer of Galinstan.

Spatial variations in magnetic permeability have been already put forward as a source of dynamo action.[15–18] In Ref. 15, by combining the effects of the soft-iron impellers and a small uniform homogeneous $\alpha_{\theta\theta}$-effect modeling the induction effects of unresolved small-scale flow fluctuations, an axisymmetric magnetic field mode was obtained in a kinematic dynamo setup. However, a uniform homogeneous α-effect is not realistic as shown in Fig. 2. In Ref. 16, the growth of the magnetic field is due to the shear of the velocity localized on the frontier between fluid and the top of the blades. The jump conditions of Sec. II B (iii) and (iv) in Ref. 16 can be interpreted as a $\mathcal{M}^\mu$ effect localized only on the blades' top. In our case, the helical flow in between the blades distorts the magnetic field and bends it along the surface of the blades and disks making the $\mathcal{M}^\mu$ term large there (as shown in Fig. 20). Therefore, it is not the dynamo mechanism described in Ref. 16 as it would occur only on the top of the blades. In Ref. 17, the solid body rotation of an anisotropic conductive or an anisotropic permeable cylindrical rotor (the anisotropy of material properties follows a logarithmic spiral shape) immersed in a static cylinder can generate an axisymmetric magnetic field. The kinematic dynamo mechanism there is due to differential rotation coupled with anisotropic diffusion. However, the generated magnetic field has a horizontal structure following spirals and a Fourier vertical structure as $\exp(ikz)$ with k the vertical wavenumber of the corresponding eigenmode, far from the VKS dynamo mode shown in Fig. 1 (right). In Ref. 18, the effect of the rotating disk is studied: by adding opposite $\alpha_{\theta\theta}$ and Ω effect above and under the disk with a higher magnetic permeability than the liquid, a decrease in the magnetic threshold is observed. However, an $\alpha_{\theta\theta}$-effect with opposite sign above and under the disk is not what is
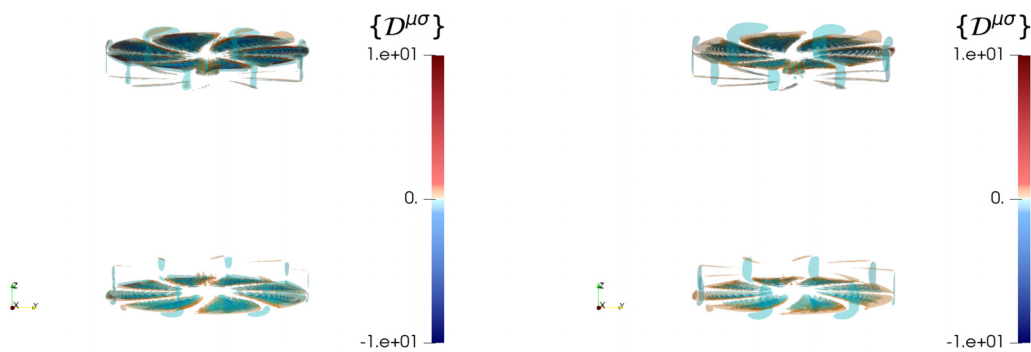

FIG. 21. Time-averaged Joule induced in-between scales magnetic transfers for the case $R_e = 1500$, $R_m = 150$, $\mu_r = 50$ in the saturated regime. Left panel: $\frac{\ell}{\eta} = 1$. Right panel: $\frac{\ell}{\eta} = 16$.
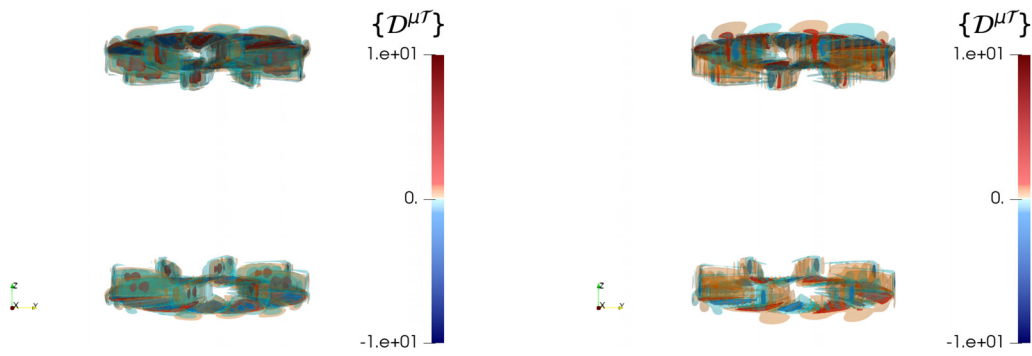
FIG. 22. Time-averaged Lorentz induced in-between scales magnetic transfers for the case $R_e = 1500, R_m = 150, \mu_r = 50$ in the saturated regime. Left panel: $\frac{\ell}{\eta} = 1$. Right panel: $\frac{\ell}{\eta} = 16$.

observed in Fig. 2. Moreover, any α-or-Ω-driven dynamo mechanism would only participate through the term $\mathcal{T}^{u \to b}$, which is globally negative in the current case $\mu_r = 50$.

Here, the main dynamo mechanism at large times for $\mu_r = 50$ is simply a self-amplifying phenomenon due to the variation of the magnetic permeability in time. Re-writing (20) by keeping only $\mathcal{M}^\mu$ gives

$$\partial_t E^m \sim E^m \partial_t \frac{1}{\mu}. \qquad (45)$$

This implies that the magnetic field grows (respectively decreases) behind (respectively in front of) the blades as can be seen in Fig. 20, which amplifies the phenomenon: stronger $\mathcal{M}^\mu$ happens where the

magnetic field is amplified. Hence, for soft-iron impellers ($\mu_r = 50$), the dynamo effect is due to rotating magnets. In the saturated regime, this is counterbalanced by both the Joule dissipation, $\mathcal{D}^\sigma$, and the energy transfer toward the velocity field, $-\mathcal{T}^{u \to b}$ (see Fig. 14).

The dynamo mechanism for steel impellers ($\mu_r = 1$) is very different as it is only due to the energy transfer from the velocity field. At the same time, it couples dynamo processes in the shear layer and the in-between blade zones (see Fig. 11).

VIII. CONCLUSION

The main result of this article is the expression on the different local transfer terms appearing in Eqs. (19) and (20). They express all
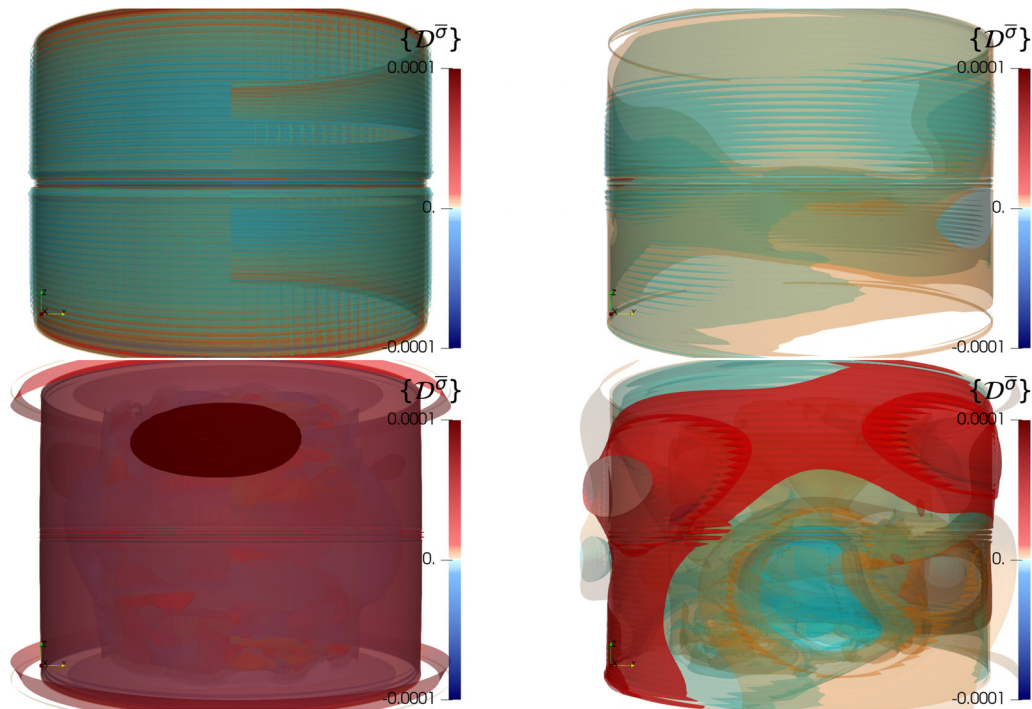

FIG. 23. Time-averaged irregular Joule dissipation in the saturated regime. Panels correspond to $\frac{\ell}{\eta} = 1$ for the first row, $\frac{\ell}{\eta} = 16$ for the second row, and the case $R_e = 1500$, $R_m = 150$, and $\mu_r = 50$ on the first column and the case $R_e = 1500$, $R_m = 300$, and $\mu_r = 1$ on the second column.

27 February 2024 16:13:02

possible exchanges between velocity and magnetic fields. Obtaining these terms was made possible by the development of a new filtering approach that can be used effectively for unstructured grids such as the finite element mesh used in SFEMaNS. We believe that this filtering method offers a general framework for the analysis of data obtained on unstructured meshes.

The viscous $\mathcal{D}^\nu$ and resistive $\mathcal{D}^\sigma$ dissipations correspond to the classical terms. The lack of smoothness of the solutions leads to the appearance of $\mathcal{D}^b$ that generalizes the anomalous dissipation $\mathcal{D}^u$ (which quantifies the kinetic energy dissipated by non-viscous means[22]) to the anomalous magnetic energy dissipation. It is rather remarkable that the combination of these anomalous dissipative terms can be written in the form of structure functions already derived in the literature[23,25] (as shown in Appendixes C and D).

The novelty is that the separation of the kinetic and magnetic energy equations allows highlighting the main terms responsible for the dynamo effect, namely, $\mathcal{T}^{u\rightarrow b}$ and $\mathcal{M}^\mu$. Using two illustrative numerical dynamo simulations with different impeller materials, we were able to show that the dynamo mechanisms are totally different when using steel or soft iron impellers. In the case of steel impellers, the only source term is the (minus) Lorentz force power $\mathcal{T}^{u\rightarrow b}$ that needs to compensate for all dissipative terms. In the case of soft iron impellers, the ferromagnetic nature of the impellers plays a crucial role in maintaining the magnetic field through $\mathcal{M}^\mu$ (and $\mathcal{D}^b$ for a filtering scale $\ell > 0$). This second mechanism cannot be described by a mean-field approach, which does not include variations in magnetic permeability nor electrical conductivity.

MHD and Navier–Stokes equations share a lot in common. However, from a mathematical perspective, it is unknown whether the viscous and resistive mechanisms that tend to smooth out potential irregularities in the velocity and magnetic field are effective enough to constrain the fields to stay smooth at all times. The analytical tools we have developed will allow us to dynamically study the rare events associated with extreme values of the anomalous dissipative terms in future work.

ACKNOWLEDGMENTS

AUTHOR DECLARATIONS
Conflict of Interest

The authors have no conflicts to disclose.

Author Contributions

Melvin Creff: Data curation (lead); Formal analysis (lead); Investigation (lead); Methodology (lead); Software (lead); Visualization (lead); Writing – original draft (lead). **Hugues Faller:** Formal analysis (supporting); Software (supporting). **Berengere Dubrulle:** Conceptualization (lead); Formal analysis (supporting); Methodology (equal); Supervision (equal); Writing – original draft (equal); Writing – review & editing (equal). **Jean Luc Guermond:** Software (equal); Supervision (supporting). **Caroline Nore:** Conceptualization (equal); Data curation (supporting); Formal analysis (supporting); Methodology (equal); Software (supporting); Supervision (lead); Writing – original draft (equal); Writing – review & editing (equal).

DATA AVAILABILITY

The data that support the findings of this study are available from the corresponding author upon reasonable request.

APPENDIX A: NAVIER–STOKES CALCULATIONS

Using the scalar product of $\rho u/2$ with Eq. (15) and the scalar product of $\rho\overline{u}^\ell/2$ with Eq. (1) leads to the equation for the transferred kinetic energy from all scales larger than ℓ to the scale ℓ,

$$\partial_t \frac{\rho u\overline{u}^\ell}{2} + \frac{\rho}{2}\left(u\partial_i\overline{u_i u}^\ell + \overline{u}^\ell\partial_i u_i u - u\nu\Delta\overline{u}^\ell \right.$$
$$\left. -\overline{u}^\ell\nu\Delta u + u\cdot\nabla\frac{\overline{p}^\ell}{\rho} + \overline{u}^\ell\cdot\nabla\frac{p}{\rho} \right)$$
$$= \frac{1}{2}(\overline{u}^\ell\cdot(j\times b) + u\cdot(\overline{j\times b}^\ell) + \rho u\cdot\overline{f}^\ell + \rho\overline{u}^\ell\cdot f). \quad \text{(A1)}$$

After some calculations, the left-hand side yields a simpler form (using multiple times $\nabla\cdot u = 0$ and $\nabla\cdot\overline{u}^\ell = 0$),

$$\frac{1}{2}\nabla\cdot(\overline{u}^\ell p + u\overline{p}^\ell) + \frac{\rho}{2}\nabla\cdot\left[(u\overline{u}^\ell)u\right] - \frac{\rho}{2}\nu\Delta(u\overline{u}^\ell)$$
$$+ \rho\nu\partial_i\overline{u_j}^\ell\partial_i u_j + \frac{\rho}{2}(u\overline{u_i\partial_i u}^\ell - u_i u\partial_i\overline{u}^\ell)$$
$$= \nabla\cdot J^{NS} + \mathcal{D}^\nu + \mathcal{D}^u. \quad \text{(A2)}$$

The first part of the right hand side can then be written as

$$\overline{u}^\ell\cdot(j\times b) + u\cdot(\overline{j\times b}^\ell) = -\left(\overline{u}^\ell\cdot(b\times j) + u\cdot(\overline{b\times j}^\ell)\right)$$
$$= -2(\mathcal{T}^{u\rightarrow b} + \mathcal{D}^b), \quad \text{(A3)}$$

while $\frac{\rho}{2}(u\cdot\overline{f}^\ell + \overline{u}^\ell\cdot f) = \mathcal{P}$.

APPENDIX B: MHD CALCULATIONS

Using the scalar product of $b/2\mu$ with Eq. (16) and the scalar product of $\overline{b}^\ell/2\mu$ with Eq. (2) leads to the equation for the transferred magnetic energy from all scales larger than ℓ to the scale ℓ,

$$\partial_t\frac{b\overline{b}^\ell}{2\mu} = \frac{1}{2\mu}\left(\overline{b}^\ell\cdot\nabla\times(u\times b) - \overline{b}^\ell\cdot\nabla\times\left(\frac{j}{\sigma}\right) + b\cdot\nabla\right.$$
$$\left. \times(\overline{u\times b}^\ell) - b\cdot\nabla\times\overline{\left(\frac{j}{\sigma}\right)}^\ell\right) - \frac{b\cdot\overline{b}^\ell}{2\mu^2}\partial_t\mu. \quad \text{(B1)}$$

The variation of the physical properties σ and μ leads to extra terms that we develop in the following.

1. Using various conductive materials

The sharp variation in the electrical conductivity at $\{r = 1.4R_{cyl}, -H/2 \le z \le H/2\}$ between the liquid sodium lateral layer ($\sigma = \sigma_0$) and the copper wall of the container ($\sigma = 4.5\sigma_0$) needs to be taken into account,

$$\frac{(\overline{b}^\ell)}{\mu} \cdot \nabla \times \left(\frac{j}{\sigma}\right) + \frac{b}{\mu} \cdot \nabla \times \overline{\left(\frac{j}{\sigma}\right)}^\ell$$

$$= \nabla \cdot \left(\frac{j}{\sigma} \times \frac{(\overline{b}^\ell)}{\mu} + \overline{\left(\frac{j}{\sigma}\right)}^\ell \times \frac{b}{\mu}\right)$$

$$+ \frac{j}{\sigma} \cdot \nabla \times \frac{(\overline{b}^\ell)}{\mu} + \overline{\left(\frac{j}{\sigma}\right)}^\ell \cdot \nabla \times \frac{b}{\mu}. \quad (B2)$$

Using

$$\overline{\left(\frac{j}{\sigma}\right)}^\ell = \frac{(\overline{j}^\ell)}{\sigma} + \overline{\left(\frac{j}{\sigma}\right)}^\ell - \frac{(\overline{j}^\ell)}{\sigma}, \quad (B3)$$

$$\nabla \times \frac{(\overline{b}^\ell)}{\mu} = \nabla \times \overline{H}^\ell + \nabla \times \frac{(\overline{b}^\ell)}{\mu} - \nabla \times \overline{H}^\ell. \quad (B4)$$

Then

$$\frac{j}{\sigma} \cdot \nabla \times \frac{(\overline{b}^\ell)}{\mu} + \overline{\left(\frac{j}{\sigma}\right)}^\ell \cdot \nabla \times \frac{b}{\mu}$$

$$= \frac{j}{\sigma} \cdot \overline{j}^\ell + \frac{j}{\sigma} \cdot \left(\nabla \times \frac{(\overline{b}^\ell)}{\mu} - \nabla \times \overline{H}^\ell\right)$$

$$+ \frac{(\overline{j}^\ell)}{\sigma} \cdot j + \left(\overline{\left(\frac{j}{\sigma}\right)}^\ell - \frac{(\overline{j}^\ell)}{\sigma}\right) \cdot j. \quad (B5)$$

Hence

$$\frac{(\overline{b}^\ell)}{\mu} \cdot \nabla \times \left(\frac{j}{\sigma}\right) + \frac{b}{\mu} \cdot \nabla \times \overline{\left(\frac{j}{\sigma}\right)}^\ell$$

$$= \nabla \cdot \left(\frac{j}{\sigma} \times \frac{(\overline{b}^\ell)}{\mu} + \overline{\left(\frac{j}{\sigma}\right)}^\ell \times \frac{b}{\mu}\right) + 2\mathcal{D}^\sigma + 2\mathcal{D}^{\mu\sigma} + 2\mathcal{D}^{\overline{\sigma}}. \quad (B6)$$

2. Using various permeable materials

The sharp variation in the magnetic permeability between the liquid sodium and the moving impellers (when $\mu \neq \mu_0$) needs to be taken into account,

$$\frac{b}{\mu} \cdot \nabla \times (\overline{u \times b}^\ell) = -\nabla \cdot \left(\frac{b}{\mu} \times (\overline{u \times b}^\ell)\right) + (\overline{u \times b}^\ell) \cdot (\nabla \times h)$$

$$= -\nabla \cdot \left(\frac{b}{\mu} \times (\overline{u \times b}^\ell)\right) + \overline{u \times b}^\ell \cdot j, \quad (B7)$$

$$\frac{(\overline{b}^\ell)}{\mu} \cdot \nabla \times (u \times b)$$

$$= -\nabla \cdot \left(\frac{(\overline{b}^\ell)}{\mu} \times (u \times b)\right) + (u \times b) \cdot \nabla \times \frac{(\overline{b}^\ell)}{\mu}$$

$$= -\nabla \cdot \left(\frac{(\overline{b}^\ell)}{\mu} \times (u \times b)\right) + (u \times b) \cdot \nabla \times \overline{H}^\ell$$

$$+ (u \times b) \cdot \left(\nabla \times \frac{(\overline{b}^\ell)}{\mu} - \nabla \times \overline{H}^\ell\right). \quad (B8)$$

Hence

$$\frac{b}{\mu} \cdot \nabla \times (\overline{u \times b}^\ell) + \frac{(\overline{b}^\ell)}{\mu} \cdot \nabla \times (u \times b)$$

$$= -\nabla \cdot \left(\frac{b}{\mu} \times (\overline{u \times b}^\ell) + \frac{(\overline{b}^\ell)}{\mu} \times (u \times b)\right)$$

$$+ 2(\mathcal{T}^{u \to b} - \mathcal{D}^b) - 2\mathcal{D}^{\mu\mathcal{T}}. \quad (B9)$$

3. Rationale for separation between $\mathcal{T}^{u \to b}$ and $\mathcal{D}^b$

By summing (20) and (19), which describe physically the time evolution of the total energy, we obtain

$$\partial_t(E^c + E^m) + \nabla \cdot J^{NS} + \nabla \cdot J^M + \mathcal{D}^\nu + \mathcal{D}^u + 2\mathcal{D}^b$$

$$+ \mathcal{D}^\sigma + \mathcal{D}^{\overline{\sigma}} + \mathcal{D}^{\mu\sigma} + \mathcal{D}^{\mu\mathcal{T}} = \mathcal{P} + \mathcal{M}^\mu.$$

On the other hand, we can subtract (20) and (19), which leads to

$$\partial_t(E^m - E^c) - \nabla \cdot J^{NS} + \nabla \cdot J^M - \mathcal{D}^\nu - \mathcal{D}^u + \mathcal{D}^\sigma$$

$$+ \mathcal{D}^{\overline{\sigma}} + \mathcal{D}^{\mu\sigma} + \mathcal{D}^{\mu\mathcal{T}} = -\mathcal{P} + 2\mathcal{T}^{u \to b} + \mathcal{M}^\mu.$$

Physically, these equations show that $\mathcal{D}^b$ is a transfer term between scales larger than ℓ and scales smaller than ℓ for the total energy (similar to $\mathcal{D}^u$ for the kinetic energy equation). Moreover, $\mathcal{D}^b$ is zero for $\ell = 0$ that would not happen if we add (or subtract) $\mathcal{D}^b$ and $\mathcal{T}^{u \to b}$. Meanwhile, $\mathcal{T}^{u \to b}$ is an energy transformation term between both energies, that does not vanish at $\ell = 0$.

It is, therefore, essential to keep the two terms separate, as adding (or subtracting) them would mix up different types of energy transfer. Moreover, calculating their sum and subtraction will always give the same number of energy transfer terms to compute and analyze.

APPENDIX C: LINKING KINETIC ENERGY TRANSFERS AND VELOCITY INCREMENTS

Following,[25] the filtering process discussed in section Sec. III E can be interpreted as a smoothing operation at a resolution ℓ achieved through the function φ_ℓ (smooth non-negative function with unit integral) such that the filtered velocity field reads

$$\overline{u_i}^\ell(\mathbf{x}, t) = \int \varphi_\ell(\mathbf{r}) u_i(\mathbf{x} + \mathbf{r}, t) d\vec{r}. \quad (C1)$$

Using increments of the velocity fields, the third-order structure function can be written as [see Eq. (2.7) in Ref. 26],

$$\left(\frac{\mathcal{D}^I}{\rho} = \right) S^{NS} = \frac{1}{4} \int (\nabla \varphi_\ell) \cdot (\delta u \delta u^2) d\vec{r}$$

$$= -\frac{1}{4} \int \varphi_\ell \nabla \cdot (\delta u \delta u^2) d\vec{r}$$

$$= -\frac{1}{4} \left[\partial_i \overline{u_i u_j u_j}^\ell - u_i \partial_i \overline{u_j u_j}^\ell - 2u_j \partial_i \overline{u_i u_j}^\ell\right.$$

$$\left.+ u_j u_j \partial_i \overline{u_i}^\ell + 2u_i u_j \partial_i \overline{u_j}^\ell\right]$$

$$= -\frac{1}{4} \left[\nabla \cdot (\overline{uu^2}^\ell - u\overline{u^2}^\ell) - 2u_j \overline{u_i \partial_i u_j}^\ell + 2u_i u_j \partial_i \overline{u_j}^\ell\right]$$

$$= -\frac{1}{4} \nabla \cdot (\overline{uu^2}^\ell - u\overline{u^2}^\ell) + \frac{1}{\rho} \mathcal{D}^u$$

$$= \frac{1}{2} \nabla \cdot J_{S^{NS}} + \frac{1}{\rho} \mathcal{D}^u, \quad (C2)$$

with $J_{S^{NS}} = -\overline{uu^2}^\ell + u\overline{u^2}^\ell$. The term S^{NS} was denoted $\mathcal{D}_\ell^I$ in Ref. 25. Note that it differs from the anomalous dissipation term $\mathcal{D}^u$ by an additional flux term (in divergence). Integrated throughout space with the proper boundary conditions, the latter should disappear but it can be responsible for localized large values on the boundaries. If we are interested in the energy injected in the small scales, the important term is $\mathcal{D}^u$.

APPENDIX D: LINKING MAGNETIC ENERGY TRANSFERS AND VELOCITY INCREMENTS

In the MHD case with $\mu \neq const.$, we introduce

$$
\begin{aligned}
S^{Mag} &= -\frac{\mu}{2}\int \varphi_\ell(\delta u \cdot \delta(b \times j) + \delta j \cdot \delta(b \times u))d\vec{r} \\
&= \frac{\mu}{2}\Big[-\overline{u \cdot (b \times j)}^\ell - \overline{j \cdot (b \times u)}^\ell + u \cdot (\overline{b \times j}^\ell) \\
&\quad + \vec{j}^\ell \cdot b \times u + j \cdot \overline{b \times u}^\ell + \overline{u}^\ell \cdot (b \times j)\Big] \\
&= \frac{\mu}{2}\Big[-u \cdot (\overline{j \times b}^\ell - \vec{j}^\ell \times b) - j \cdot (\overline{u \times b}^\ell - \overline{u}^\ell \times b)\Big] \\
&= 2\mu\mathcal{D}^b.
\end{aligned}
\tag{D1}
$$

In the special case $\mu = const.$, this formula simplifies like in Ref. 23

$$
\begin{aligned}
\tilde{S}^{Mag} &= \frac{1}{4}\int(\nabla\varphi_\ell) \cdot (\delta u \delta b^2 - 2(\delta u \cdot \delta b)\delta b)d\vec{r} \\
&= -\frac{1}{4}\int \varphi_\ell \nabla \cdot (\delta u \delta b^2 - 2(\delta u \cdot \delta b)\delta b)d\vec{r}.
\end{aligned}
\tag{D2}
$$

Treating both parts of the integral independently

$$
\begin{aligned}
&-\int \varphi_\ell \nabla \cdot (\delta u \delta b^2)d\vec{r} \\
&= -\nabla \cdot (\overline{ub^2}^\ell) + 2b_j\partial_i(\overline{u_i b_j}^\ell) + u_i\partial_i(\overline{b_j b_j}^\ell) \\
&\quad - b_j b_j \partial_i(\overline{u_i}^\ell) - 2b_j u_i \partial_i(\overline{b_j}^\ell) \\
&= -\nabla \cdot (\overline{ub^2}^\ell + \overline{u}^\ell b^2 + u(\overline{b}^\ell \cdot b)) \\
&\quad + 2b_j\overline{u_i\partial_i(b_j)}^\ell + 2u_i\overline{b_j\partial_i(b_j)}^\ell + 2b_j\overline{u_i}^\ell\partial_i(b_j) + 2\overline{b_j}^\ell u_i\partial_i b_j.
\end{aligned}
\tag{D3}
$$

$$
\begin{aligned}
&\int \varphi_\ell \nabla \cdot ((\delta u \cdot \delta b)\delta b)d\vec{r} \\
&= \nabla \cdot (\overline{(u \cdot b)b}^\ell) + b_i\partial_i(\overline{u_j b_j}^\ell) + u_j\partial_i(\overline{b_i b_j}^\ell) + b_j\partial_i(\overline{u_j b_i}^\ell) \\
&\quad + b_i b_j \partial_i(\overline{u_j}^\ell) + b_i u_j \partial_i(\overline{b_j}^\ell) + b_j u_j \partial_i(\overline{b_i}^\ell) \\
&= \nabla \cdot (\overline{(u \cdot b)b}^\ell + b_i\overline{u_j b_j}^\ell + b_i b_j \overline{u_j}^\ell + b_i u_j \overline{b_j}^\ell) \\
&\quad - u_j\overline{b_i\partial_i(b_j)}^\ell - b_j\overline{b_i\partial_i(u_j)}^\ell - \overline{u_j}^\ell b_i\partial_i(b_j) - \overline{b_j}^\ell b_i\partial_i(u_j).
\end{aligned}
\tag{D4}
$$

Grouping two by two similar terms

$$
\begin{aligned}
&b_j\overline{u_i\partial_i(b_j)}^\ell - b_j\overline{b_i\partial_i(u_j)}^\ell \\
&= b \cdot \nabla \times (\overline{b \times u}^\ell) = \nabla \times b \cdot \overline{b \times u}^\ell - \nabla \cdot (b \times (\overline{b \times u}^\ell)),
\end{aligned}
\tag{D5}
$$

$$
\begin{aligned}
&\overline{b_j}^\ell u_i\partial_i b_j - \overline{b_j}^\ell b_i\partial_i(u_j) = \overline{b}^\ell \cdot \nabla \times (b \times u) \\
&= \overline{\nabla \times b}^\ell \cdot b \times u - \nabla \cdot (\overline{b}^\ell \times (b \times u)),
\end{aligned}
\tag{D6}
$$

$$
u_i\overline{b_j\partial_i(b_j)}^\ell - u_j\overline{b_i\partial_i(b_j)}^\ell = u \cdot (\overline{b \times (\nabla \times b)}^\ell),
\tag{D7}
$$

$$
b_j\overline{u_i}^\ell\partial_i(b_j) - \overline{u_j}^\ell b_i\partial_i(b_j) = \overline{u}^\ell \cdot (b \times (\nabla \times b)),
\tag{D8}
$$

using that for fields of null divergence

$$
\nabla \times (A \times B) = (B \cdot \nabla)A - (A \cdot \nabla)B = B_i\partial_i A_j - A_i\partial_i B_j,
\tag{D9}
$$

$$
B \times (\nabla \times B) = \frac{1}{2}\nabla B^2 - (B \cdot \nabla)B = B_i\partial_j B_i - B_i\partial_i B_j.
\tag{D10}
$$

On the other hand

$$
\begin{aligned}
4\mathcal{D}^b &= -u \cdot (\overline{j \times b}^\ell - \vec{j}^\ell \times b) - j \cdot (\overline{u \times b}^\ell - \overline{u}^\ell \times b) \\
&= u \cdot (\overline{b \times j}^\ell) + \vec{j}^\ell \cdot b \times u + j \cdot \overline{b \times u}^\ell + \overline{u}^\ell \cdot (b \times j).
\end{aligned}
\tag{D11}
$$

Hence, by regrouping all terms with a divergence in a current, and using $\nabla \times b = \mu j$ and $\overline{\nabla \times b}^\ell = \mu\vec{j}^\ell$ (because $\mu = const.$)

$$
2\mu\mathcal{D}^b = \tilde{S}^{Mag} - \frac{1}{2}\nabla \cdot J_{S^{Mag}},
\tag{D12}
$$

with

$$
\begin{aligned}
J_{S^{Mag}} &= \overline{b}^\ell \times (b \times u) + b \times (\overline{b \times u}^\ell) - \overline{(u \cdot b)b}^\ell \\
&\quad - b(\overline{u \cdot b}^\ell) - b(b \cdot \overline{u}^\ell) - b(u \cdot \overline{b}^\ell) \\
&\quad + \frac{1}{2}\overline{ub^2}^\ell + \frac{1}{2}\overline{u}^\ell b^2 + \frac{1}{2}u(\overline{b}^\ell \cdot b).
\end{aligned}
\tag{D13}
$$

So, in this special case

$$
S^{Mag} = \tilde{S}^{Mag} - \frac{1}{2}\nabla \cdot J_{S^{Mag}}.
\tag{D14}
$$

APPENDIX E: DETAILS ON THE NUMERICS AND VON KÁRMÁN SYMMETRIES

1. Numerical setup

The numerical setup corresponds to the von Kármán swirling flow. The symmetries of this setup are presented in Subsection 4 of Appendix E. We have performed MHD simulations of this setup on various supercomputers[21] (up to about 2000 cores on the IDRIS supercomputer), allowing us to reach kinetic Reynolds number up to 10^5 and magnetic Reynolds number of the order of a few hundred, resulting in a magnetic Prandtl number around 10^{-3}.

2. SFEMaNS code

The SFEMaNS code integrates the system of coupled Eqs. (1)–(4). It uses a hybrid spatial discretization combining finite elements and spectral decomposition. For the hydrodynamic part, the approximation in space is done by using a Fourier decomposition in the azimuthal direction and the continuous Hood-Taylor Lagrange element $\mathbb{P}_1$–$\mathbb{P}_2$ in the meridian section (quadratic approximation

for the velocity field and linear approximation for pressure). All the discrete scalar functions f are written in the generic form

$$f(r, \theta, z, t) = f_h^{c,0}(r, z, t) + \sum_{m_F=1}^{M} f_h^{c,m_F}(r, z, t) \cos(m_F \theta)$$
$$+ \sum_{m_F=1}^{M} f_h^{s,m_F}(r, z, t) \sin(m_F \theta), \qquad (E1)$$

with (r, θ, z) the cylindrical coordinates, t the time and M the number of Fourier azimuthal modes considered. The functions f_h^{c,m_F} and f_h^{s,m_F} belong to a finite element space with h the typical mesh-size. The approximation in time is done by using a pressure-correction method.[39] The moving counter-rotating impellers are accounted for by using a pseudo-penalty technique described in Ref. 40 Modulo the computations of nonlinear terms with the fast Fourier transform, the linear problems at each time step for each Fourier mode in the meridian section are uncoupled and are thereby parallelized by using the message passing interface. The solution of each linear problem in the meridian section is further parallelized by using graph partitioning techniques from the METIS library[41] and subroutines from the portable extensible toolkit for scientific computation library (PETSc),[42] for the linear algebra. For the magnetic part, the algorithm solves the problem using the magnetic induction b in the conducting region (after standard elimination of the electric field) and the scalar magnetic potential in the insulating exterior. The fields in each region are approximated by using H^1-conforming Lagrange elements with a penalty technique to control the divergence of b in a negative Sobolev norm that guarantees convergence under minimal regularity (see details in Ref. 43, (Sec. III B), Ref. 44) The coupling between conducting and insulating media is done by using an interior penalty method. SFEMaNS has been thoroughly validated on numerous manufactured solutions and against other MHD codes (see, e.g., Refs. 45 and 46).

3. Description of the numerical runs

In this paper, we focus on two series of runs described in Ref. 21 (Table III). We use non-dimensional units such that the reference length L_{ref} is set to the inner cylinder radius R_{cyl}. Denoting by σ_0 the electrical conductivity of the liquid sodium, ρ its density, and μ_0 the magnetic permeability of vacuum, the magnetic induction is made non-dimensional by using the Alfvén scaling $B = U\sqrt{\rho\mu_0}$, with $U = \omega R_{cyl}$ where ω is the angular velocity of the impellers. The two governing parameters are $R_m = \mu_0 \sigma_0 R_{cyl}^2 \omega$, the magnetic Reynolds number, and $R_e = R_{cyl}^2 \omega / \nu$, the kinetic Reynolds number, with ν the kinematic viscosity of the fluid. We define a relative electrical conductivity σ_r and a relative magnetic permeability μ_r. These quantities are not constant since the walls and the impellers are made of different materials like copper, steel, and soft iron. Specifically, we define $\sigma_r = 1, \mu_r = 1$ in the region $\{(r, \theta, z) \in [1, 1.4] \times [0, 2\pi] \times [-1, 1]\}$ to model the lateral layer of stagnant liquid sodium, and $\sigma_r = 4.5, \mu_r = 1$ in $\{(r, \theta, z) \in [1.4, 1.6] \times [0, 2\pi] \times [-1, 1]\}$ to represent the lateral copper wall. The computations are performed with 128 Fourier modes and a non-uniform meridian mesh, with minimal spacing $h_{min} = 2.5 \times 10^{-3}$ and maximal spacing $h_{max} = 10^{-2}$ leading to an averaged meridian mesh $h_{mean} = 7.92 \times 10^{-3}$. We can estimate the

Kolmogorov scale $\eta = (\nu^3/\epsilon)^{1/4}$ using the kinematic viscosity $\nu = 1/R_e$ and the energy dissipation rate $\epsilon = 2R_{cyl}K_p/\pi H$ (with K_p the time-averaged torque applied by the impellers to the fluid and $H = 2$ the total height of the container). Table II of Ref. 21 provides $K_p = 5.08 \times 10^{-2}$ at $R_e = 1500$ resulting in $\eta = 1.16 \times 10^{-2}$.

4. Symmetries of the von Kármán flow and implications for the Ω and α terms

The von Kármán flow with exactly counter-rotating impellers has one particular symmetry that can provide information about the spatial distribution of instantaneous and averaged quantities based on the velocity field. It is called the R_π symmetry[47] and corresponds to a symmetry of rotation of π about any horizontal axis,

$$R_\pi \begin{pmatrix} u_r \\ u_\theta \\ u_z \end{pmatrix}(r, \theta, z) = \begin{pmatrix} u_r \\ -u_\theta \\ -u_z \end{pmatrix}(r, -\theta, -z), \qquad (E2)$$

where $u = (u_r, u_\theta, u_z)$ is the velocity vector in cylindrical coordinates with r the radial distance, θ the azimuthal angle and z the height. Another symmetry, apart from the impellers, is axisymmetry about the z axis defined as

$$S_{\theta_0} \begin{pmatrix} u_r \\ u_\theta \\ u_z \end{pmatrix}(r, \theta, z) = \begin{pmatrix} u_r \\ u_\theta \\ u_z \end{pmatrix}(r, \theta + \theta_0, z). \qquad (E3)$$

Based on (E2), one can deduce that, for a velocity field symmetric under the R_π symmetry, the Ω-terms satisfy

$$\Omega_r'(r, \theta, z) = -\Omega_r'(r, -\theta, -z)$$

and

$$\Omega_z'(r, \theta, z) = +\Omega_z'(r, -\theta, -z). \qquad (E4)$$

For the α-tensor (11), one needs the expression for the velocity gradient tensor in cylindrical coordinates,

$$\nabla u = \begin{pmatrix} \dfrac{\partial u_r}{\partial r} & \dfrac{1}{r}\dfrac{\partial u_r}{\partial \theta} - \dfrac{u_\theta}{r} & \dfrac{\partial u_r}{\partial z} \\ \dfrac{\partial u_\theta}{\partial r} & \dfrac{1}{r}\dfrac{\partial u_\theta}{\partial \theta} + \dfrac{u_r}{r} & \dfrac{\partial u_\theta}{\partial z} \\ \dfrac{\partial u_z}{\partial r} & \dfrac{1}{r}\dfrac{\partial u_z}{\partial \theta} & \dfrac{\partial u_z}{\partial z} \end{pmatrix}. \qquad (E5)$$

Using (E5) in the helicity tensor, one can infer that, for a velocity field symmetric under the R_π symmetry, the helicity tensor satisfies

$$\begin{pmatrix} h_{rr} & h_{r\theta} & h_{rz} \\ h_{\theta r} & h_{\theta\theta} & h_{\theta z} \\ h_{zr} & h_{z\theta} & h_{zz} \end{pmatrix}(r, \theta, z) = \begin{pmatrix} +h_{rr} & -h_{r\theta} & -h_{rz} \\ -h_{\theta r} & +h_{\theta\theta} & +h_{\theta z} \\ -h_{zr} & +h_{z\theta} & +h_{zz} \end{pmatrix}(r, -\theta, -z). \qquad (E6)$$

The α-tensor will follow the same rules.

APPENDIX F: FILTERING ISSUES

We examine the issues related to the filtering process concerning the boundaries and its non-commutation with derivatives. We start with Eq. (40) in a domain $\mathcal{D} \subset \mathbb{R}^3$ with boundary $\partial\mathcal{D}$

$$(1 - \ell^2 \Delta)\overline{f_i}^{\ell} = f_i. \tag{F1}$$

The weak formulation is obtained using test functions ϕ_i,

$$\int_{\mathcal{D}} \left[(1 - \ell^2 \Delta)\overline{f_i}^{\ell} \right] \phi_i = \int_{\mathcal{D}} f_i \phi_i$$
$$\Longleftrightarrow \int_{\mathcal{D}} \overline{f_i}^{\ell} \phi_i + \int_{\mathcal{D}} \ell^2 (\nabla_k \overline{f_i}^{\ell})(\nabla_k \phi_i) - \int_{\partial \mathcal{D}} \ell^2 n_k (\nabla_k \overline{f_i}^{\ell}) \phi_i = \int_{\mathcal{D}} f_i \phi_i.$$

This is the formulation used in SFEMANS to solve these equations.

1. Discontinuous Galerkin method

This section explains how to solve the filtering equation at the interface between the velocity mesh and the magnetic field mesh (that includes the velocity mesh). This is needed in order for both meshes to communicate; otherwise, the filter would create a discontinuity in the filtered field at the interface between the meshes.

Let us consider a domain $\mathcal{D} \subset \mathbb{R}^3$ with boundary $\partial \mathcal{D}$. The domain is assumed to be partitioned in two subdomains $\mathcal{D}_1$ and $\mathcal{D}_2$ such that $\overline{\mathcal{D}} = \overline{\mathcal{D}_1} \cup \overline{\mathcal{D}_2}$, $\mathcal{D}_1 \cap \mathcal{D}_2 = \varnothing$. The interface between both domains is denoted by $\Sigma = \overline{\mathcal{D}_1} \cap \overline{\mathcal{D}_2}$,

$$\int_{\mathcal{D}_1 \cup \mathcal{D}_2} \left[(1 - \ell^2 \Delta)\overline{f_i}^{\ell} \right] \phi_i = \int_{\mathcal{D}_1 \cup \mathcal{D}_2} f_i \phi_i$$
$$\Longleftrightarrow \int_{\mathcal{D}_1 \cup \mathcal{D}_2} \overline{f_i}^{\ell} \phi_i + \int_{\mathcal{D}_1 \cup \mathcal{D}_2} \ell^2 (\nabla_k \overline{f_i}^{\ell})(\nabla_k \phi_i) - \int_{\partial \mathcal{D}} \ell^2 n_k (\nabla_k \overline{f_i}^{\ell}) \phi_i$$
$$- \int_{\Sigma} \left(\ell^2 n_{1k} (\nabla_k \overline{f_{1i}}^{\ell}) \phi_{1i} + \ell^2 n_{2k} (\nabla_k \overline{f_{2i}}^{\ell}) \phi_{2i} \right) = \int_{\mathcal{D}_1 \cup \mathcal{D}_2} f_i \phi_i.$$

The vector n_i is the outward normal vector to the interface Σ with respect to $\mathcal{D}_i$.

Using $(a_1 b_1 + a_2 b_2) = \frac{1}{2}[(a_1 + a_2)(b_1 + b_2) + (a_1 - a_2)(b_1 - b_2)]$

$$\int_{\Sigma} \left(n_{1k}(\nabla_k \overline{f_{1i}}^{\ell}) \phi_{1i} + n_{2k}(\nabla_k \overline{f_{2i}}^{\ell}) \phi_{2i} \right)$$
$$= \int_{\Sigma} \frac{1}{2} \left((n_{1k} \nabla_k \overline{f_{1i}}^{\ell} + n_{2k} \nabla_k \overline{f_{2i}}^{\ell})(\phi_{1i} + \phi_{2i}) \right.$$
$$\left. + (n_{1k} \nabla_k \overline{f_{1i}}^{\ell} - n_{2k} \nabla_k \overline{f_{2i}}^{\ell})(\phi_{1i} - \phi_{2i}) \right)$$
$$= \int_{\Sigma} \frac{1}{2} \left(n_{1k} ||\nabla_k \overline{f_i}^{\ell}|| \{\phi_i\} + n_{1k} \{\nabla_k \overline{f_i}^{\ell}\} ||\phi_i|| \right),$$

using $n_{2k} = -n_{1k}$ and defining $||f_i|| = (f_{1i} - f_{2i})$ and $\{f_i\} = (f_{1i} + f_{2i})$.

In cylindrical coordinates, we have

$$n_k(\nabla_k \overline{f_i}^{\ell}) \phi_i = \begin{vmatrix} (n_r \partial_r + n_z \partial_z)\overline{f_r}^{\ell} \\ (n_r \partial_r + n_z \partial_z)\overline{f_\theta}^{\ell} \\ (n_r \partial_r + n_z \partial_z)\overline{f_z}^{\ell} \end{vmatrix} \cdot \begin{vmatrix} \phi_r \\ \phi_\theta \\ \phi_z \end{vmatrix}.$$

For regularization purpose, the following term is added:

$$\int_{\Sigma} \frac{\beta}{h} (\overline{f_{1i}}^{\ell} - \overline{f_{2i}}^{\ell})(\phi_{1i} - \phi_{2i}) = \int_{\Sigma} \frac{\beta}{h} ||\overline{f_i}^{\ell}|| ||\phi_i||,$$

where h represents the mesh size and β a tunable penalty parameter that is always set to one in our numerical investigations.

The final implemented equation is

$$\int_{\mathcal{D}_1 \cup \mathcal{D}_2} \overline{f_i}^{\ell} \phi_i + \int_{\mathcal{D}_1 \cup \mathcal{D}_2} \ell^2 (\nabla_k \overline{f_i}^{\ell})(\nabla_k \phi_i) - \int_{\partial \mathcal{D}} \ell^2 n_k (\nabla_k \overline{f_i}^{\ell}) \phi_i$$
$$- \int_{\Sigma} \frac{\ell^2}{2} \left(n_{1k} ||\nabla_k \overline{f_i}^{\ell}|| \{\phi_i\} + n_{1k} \{\nabla_k \overline{f_i}^{\ell}\} ||\phi_i|| \right)$$
$$+ \int_{\Sigma} \frac{\beta}{h} ||\overline{f_i}^{\ell}|| ||\phi_i|| = \int_{\mathcal{D}_1 \cup \mathcal{D}_2} f_i \phi_i. \tag{F2}$$

Note that, when $\ell = 0$, we get $\overline{f_i}^0 = f_i$ as needed. When $\ell \neq 0$, the impact of the boundaries ($\partial \mathcal{D}$, Σ) scales like ℓ^2.

2. Non-commutation of filter and derivatives

In this section, we study commutation between filtering and derivatives. As an example, we study the case where we derive according to one direction X. The equation to filter such a derivative would be

$$(1 - \ell^2 \Delta)\overline{\partial_X f_i}^{\ell} = \partial_X f_i, \tag{F3}$$

with its weak formulation being

$$\int_{\mathcal{D}} \left[(1 - \ell^2 \Delta)\overline{\partial_X f_i}^{\ell} \right] \phi_i = \int_{\mathcal{D}} (\partial_X f_i) \phi_i. \tag{F4}$$

Working on the rhs gives

$$\int_{\mathcal{D}} (\partial_X f_i) \phi_i$$
$$= -\int_{\mathcal{D}} f_i (\partial_X \phi_i) + \int_{\partial \mathcal{D}} f_i \phi_i$$
$$= -\int_{\mathcal{D}} \left[(1 - \ell^2 \Delta)\overline{f_i}^{\ell} \right] \partial_X \phi_i + \int_{\partial \mathcal{D}} f_i \phi_i$$
$$= \int_{\mathcal{D}} \left[\partial_X (1 - \ell^2 \Delta)\overline{f_i}^{\ell} \right] \phi_i - \int_{\partial \mathcal{D}} \left[(1 - \ell^2 \Delta)\overline{f_i}^{\ell} \right] \phi_i + \int_{\partial \mathcal{D}} f_i \phi_i$$
$$= \int_{\mathcal{D}} \left[(1 - \ell^2 \Delta)\partial_X \overline{f_i}^{\ell} \right] \phi_i + \int_{\partial \mathcal{D}} \ell^2 (\Delta \overline{f_i}^{\ell}) \phi_i + \int_{\partial \mathcal{D}} (f_i - \overline{f_i}^{\ell}) \phi_i.$$

Hence

$$\int_{\mathcal{D}} \left[(1 - \ell^2 \Delta)(\overline{\partial_X f_i}^{\ell} - \partial_X \overline{f_i}^{\ell}) \right] \phi_i = \int_{\partial \mathcal{D}} (f_i - \overline{f_i}^{\ell}) \phi_i + \int_{\partial \mathcal{D}} \ell^2 (\Delta \overline{f_i}^{\ell}) \phi_i. \tag{F5}$$

When $\ell = 0$, the filter and derivatives commute if Dirichlet boundary conditions are used (vanishing of the first rhs term). In contrast, when $\ell \neq 0$, there are errors which scale like ℓ^2 on the boundaries $\partial \mathcal{D}$ as indicated by the second rhs term in ℓ^2. This means that, as long as we are interested in derivatives away from the edges $\geq \ell^2$, the error introduced by commutating derivatives and filtering is negligible.

REFERENCES

[1]H. Moffatt, *Magnetic Field Generation in Electrically Conducting Fluids* (Cambridge University Press, 1978).
[2]F. Krause and K.-H. Radler, *Mean-Field Magnetohydrodynamics and Dynamo Theory* (Pergamon Press Oxford, 1980).
[3]R. Stieglitz and U. Müller, Phys. Fluids **13**, 561 (2001).
[4]A. Gailitis, O. Lielausis, E. Platacis, S. Dement'ev, A. Cifersons, G. Gerbeth, T. Gundrum, F. Stefani, M. Christen, and G. Will, Phys. Rev. Lett. **86**, 3024 (2001).

[5]R. Monchaux, M. Berhanu, M. Bourgoin, M. Moulin, P. Odier, J.-F. Pinton, R. Volk, S. Fauve, N. Mordant, F. Pétrélis, A. Chiffaudel, F. Daviaud, B. Dubrulle, C. Gasquet, L. Marié, and F. Ravelet, Phys. Rev. Lett. **98**, 044502 (2007).

[6]S. Miralles, N. Bonnefoy, M. Bourgoin, P. Odier, J.-F m c Pinton, N. Plihon, G. Verhille, J. Boisson, F. M. C. Daviaud, and B. Dubrulle, Phys. Rev. E **88**, 013002 (2013).

[7]J.-P. Laval, P. Blaineau, N. Leprovost, B. Dubrulle, and F. Daviaud, Phys. Rev. Lett. **96**, 204503 (2006).

[8]A. Alexakis, S. Fauve, C. Gissinger, and F. Pétrélis, J. Plasma Phys. **84**, 735840401 (2018).

[9]F. Pétrélis, N. Mordant, and S. Fauve, Geophys. Astrophys. Fluid Dyn. **101**, 289 (2007).

[10]C. J. P. Gissinger, Europhys. Lett. **87**, 39002 (2009).

[11]F. Ravelet, B. Dubrulle, F. Daviaud, and P.-A. Ratié, Phys. Rev. Lett. **109**, 024503 (2012).

[12]F. H. Busse and J. Wicht, Geophys. Astrophys. Fluid Dyn. **64**, 135 (1992).

[13]T. M. Rogers and J. N. McElwaine, Astrophys. J. Lett. **841**, L26 (2017).

[14]F. Marcotte, B. Gallet, F. M. C. Pétrélis, and C. Gissinger, Phys. Rev. E **104**, 015110 (2021).

[15]A. Giesecke, F. Stefani, and G. Gerbeth, Phys. Rev. Lett. **104**, 044503 (2010).

[16]B. Gallet, F. Pétrélis, and S. Fauve, J. Fluid Mech. **727**, 161–190 (2013).

[17]F. Plunian and T. Alboussière, J. Plasma Phys. **87**, 905870110 (2021).

[18]J. Herault and F. Pétrélis, Phys. Rev. E **90**, 033015 (2014).

[19]J. Varela, S. Brun, B. Dubrulle, and C. Nore, Phys. Rev. E **92**, 063015 (2015).

[20]J. Varela, S. Brun, B. Dubrulle, and C. Nore, Phys. Plasmas **24**, 053518 (2017).

[21]C. Nore, D. Castanon, L. Cappanera, and J.-L. Guermond, J. Fluid Mech. **854**, 164 (2018).

[22]J. Duchon and R. Robert, Nonlinearity **13**, 249 (1999).

[23]S. Galtier, J. Phys. A: Math. Theor. **51**, 205501 (2018).

[24]V. David, S. Galtier, F. Sahraoui, and L. Z. Hadid, Astrophys. J. **927**, 200 (2022).

[25]B. Dubrulle, J. Fluid Mech. **867**, P1 (2019).

[26]H. Faller, D. Geneste, T. Chaabo, A. Cheminet, V. Valori, Y. Ostovan, L. Cappanera, C. Cuvier, F. Daviaud, J.-M. Foucaut et al., J. Fluid Mech. **914**, A2 (2021).

[27]H. Faller, "Dissipation, cascades et singularités en turbulence," Ph.D. thesis (ED-PIF, 2018–2021).

[28]G. L. Eyink, Phys. Rev. E **83**, 056405 (2011).

[29]S. Childress, Topological Aspects of the Dynamics of Fluids and Plasmas, edited by H. K. Moffatt, G. M. Zaslavsky, P. Comte, and M. Tabor (Springer, Dordrecht, 1992).

[30]G. L. Eyink, Phys. Rev. X **8**, 041020 (2018).

[31]V. David and S. Galtier, Phys. Rev. E **103**, 063217 (2021).

[32]P. Debue, V. Valori, C. Cuvier, F. Daviaud, J.-M. Foucaut, J.-P. Laval, C. Wiertel-Gasquet, V. Padilla, and B. Dubrulle, J. Fluid Mech. **A9**, 914 (2021).

[33]S. Kreuzahler, Y. Ponty, N. Plihon, H. Homann, and R. Grauer, Phys. Rev. Lett. **119**, 234501 (2017).

[34]R. Laguerre, C. Nore, A. Ribeiro, J. Léorat, J.-L. Guermond, and F. Plunian, Phys. Rev. Lett. **101**, 104501 (2008).

[35]R. Laguerre, C. Nore, A. Ribeiro, J. Léorat, J.-L. Guermond, and F. Plunian, Phys. Rev. Lett. **101**, 219902 (2008).

[36]E. W. Saw, D. Kuzzay, D. Faranda, A. Guittoneau, F. Daviaud, C. Wiertel-Gasquet, V. Padilla, and B. Dubrulle, Nat. Commun. **7**, 12466 (2016).

[37]R. Alejandro Avalos-Zúñiga and J. Priede, Proc. Roy. Soc. A **479**, 20220740 (2023).

[38]T. Alboussière, F. Plunian, and M. Moulin, Proc. Roy. Soc. A **478**, 20220374 (2022).

[39]J.-L. Guermond, P. Minev, and J. Shen, Comput. Methods Appl. Mech. Eng. **195**, 6011 (2006).

[40]R. Pasquetti, R. Bwemba, and L. Cousin, Appl. Numer. Math. **58**, 946 (2008).

[41]G. Karypis and V. Kumar, SIAM J. Sci. Comput. **20**, 359 (1998).

[42]S. Balay, W. Gropp, L. C. McInnes, and B. Smith, Report No. ANL-95/11 (Argonne National Laboratory, 1998).

[43]A. Giesecke, C. Nore, F. Stefani, G. Gerbeth, J. Léorat, F. Luddens, and J.-L. Guermond, Geophys. Astrophys. Fluid Dyn. **104**, 505 (2010).

[44]A. Bonito, J.-L. Guermond, and F. Luddens, J. Math. Anal. Appl. **408**, 498 (2013).

[45]A. Giesecke, C. Nore, F. Stefani, G. Gerbeth, J. Léorat, W. Herreman, F. Luddens, and J.-L. Guermond, New J. Phys. **14**, 053005 (2012).

[46]P. Marti, N. Schaeffer, R. Hollerbach, D. Cébron, C. Nore, F. Luddens, J.-L. Guermond, J. Aubert, S. Takehiro, Y. Sasaki, Y.-Y. Hayashi, R. Simitev, F. Busse, S. Vantieghem, and A. Jackson, Geophys. J. Int. **197**, 119 (2014).

[47]C. Nore, L. S. Tuckerman, O. Daube, and S. Xin, J. Fluid Mech. **477**, 51 (2003).

27 February 2024 16:13:02